

Synthesis and characterisation of light lanthanide *bis*-phospholyl borohydride complexes

Jingjing Liu, Lydia E. Nodaraki, Philip J. Cobb, Marcus J. Giansiracusa, Fabrizio Ortu, Floriana Tuna and David P. Mills*

Department of Chemistry, School of Natural Sciences, The University of Manchester, Manchester, M13 9PL, UK.

Contents

1. Synthesis of 1-Ln, 2-Ln and 3-Ce	S2
2. Crystallography	S6
3. Molecular structures of complexes 1-La, 1-Ce, 1-Nd and 1-Sm	S7
4. Molecular structures of complexes 2-La, 2-Ce and 3-Ce.....	S12
5. NMR spectroscopy	S15
6. ATR-IR spectroscopy	S35
7. UV-vis-NIR spectroscopy	S40
8. Magnetism	S45
9. CASSCF-SO Results.....	S48
10. References.....	S52

1. Synthesis of 1-Ln, 2-Ln and 3-Ce

[La(Htp)₂(μ-BH₄)] (1-La). Di-*n*-butyl ether (20 mL) was added to a pre-cooled (−78 °C) Rotaflow tap-appended ampoule containing [La(BH₄)₃(THF)_{3.5}] (0.872 g, 2 mmol) and K(Htp) (0.937 g, 4 mmol). The reaction mixture was refluxed for 16 hours, allowed to settle and filtered. The solution was concentrated to 2 mL and stored at −25 °C overnight to afford **1-La** as colourless crystals (0.341 g, 31%). Anal calcd (%) for C₄₈H₈₈B₂La₂P₄: C, 52.92; H, 8.15. Found (%): C, 51.12; H, 8.17. ¹H NMR (C₆D₆, 400 MHz, 298 K): δ = 1.52 (72H, C(CH₃)₃), 7.35 (8H, Htp-CH), BH₄ signals could not be observed. ¹¹B{¹H} NMR (C₆D₆, 128 MHz, 298 K): δ = −20.89 (BH₄). ¹¹B NMR (C₆D₆, 128 MHz, 298 K): δ = −20.91 (br q, ¹J_{BH} = 84.1 Hz, BH₄). ¹³C{¹H} NMR (C₆D₆, 100 MHz, 298 K): δ = 34.50 (d, ³J_{PC} = 6.9 Hz, C(CH₃)₃), 37.02 (d, ²J_{PC} = 15.7 Hz, C(CH₃)₃), 125.01 (s, Htp-CH), 178.08 (d, ¹J_{PC} = 59.7 Hz, PC). ³¹P{¹H} NMR (C₆D₆, 162 MHz, 298 K): δ = 105.65 (Htp-P). FTIR (ATR, microcrystalline): $\tilde{\nu}$ = 2957 (s), 2900 (m), 2864 (m), 2375 (br, w, B-H str.), 2274 (br, m, B-H str.), 2208 (br, w, B-H str.), 1473 (s), 1460 (s), 1416 (w), 1391 (s), 1359 (s), 1301 (w), 1247 (s), 1194 (s), 1151 (br, m), 1115 (br, s), 1065 (s), 1037 (s), 1020 (w), 991 (s), 920 (w), 888 (w), 817 (s), 794 (s), 720 (s), 660 (s), 611 (s), 590 (s), 517 (w), 429 (w) cm^{−1}.

[Ce(Htp)₂(μ-BH₄)₂] (1-Ce). Di-*n*-butyl ether (20 mL) was added to a pre-cooled (−78 °C) Rotaflow tap-appended ampoule containing [Ce(BH₄)₃(THF)_{3.5}] (0.874 g, 2 mmol) and K(Htp) (0.937 g, 4 mmol). The reaction mixture was refluxed for 16 hours, allowed to settle and filtered. The solution was concentrated to 2 mL and stored at −25 °C overnight to afford **1-Ce** as orange crystals (0.442 g, 41%). Anal calcd (%) for C₄₈H₈₈B₂Ce₂P₄: C, 52.80; H, 8.13. Found (%): C, 51.80; H, 8.11. μ_{eff} (Evans method, 298 K, C₆D₆): 3.43 μ_B. ¹H NMR (C₆D₆, 400 MHz, 298 K): δ = −35.05 (br, 8H, $\nu_{1/2}$ ~ 1400 Hz, BH₄), −4.63 (br, 4H, $\nu_{1/2}$ = 60 Hz, Htp-CH), −3.70 (br, 72H, $\nu_{1/2}$ = 20 Hz, C(CH₃)₃), −2.64 (br, 4H, $\nu_{1/2}$ = 60 Hz, Htp-CH). ¹¹B{¹H} NMR (C₆D₆, 128 MHz, 298 K): δ = −3.90 (BH₄). The paramagnetism of **1-Ce** precluded assignment of its ¹³C{¹H} and ³¹P{¹H} NMR spectra. FTIR (ATR, microcrystalline): $\tilde{\nu}$ = 2948 (br, m), 2872 (br, m), 1644 (m), 1513 (s), 1459 (s), 1383 (br, m), 1276 (m), 1246 (w), 1084 (s), 977 (s), 878 (br, s), 866 (br, s), 820 (w), 796 (w), 774 (s), 740 (s), 705 (s), 683 (s), 661 (s), 636 (s), 611 (m), 554 (w), 521 (w), 422 (w) cm^{−1}.

[Nd(Htp)₂(μ-BH₄)₂ (1-Nd). Di-*n*-butyl ether (20 mL) was added to a pre-cooled (−78 °C) Rotaflow tap-appended ampoule containing [Nd(BH₄)₃(THF)_{3.5}] (0.882 g, 2 mmol) and K(Htp) (0.937 g, 4 mmol). The reaction mixture was refluxed for 16 hours, allowed to settle and filtered. The solution was concentrated to 2 mL and stored at −25 °C overnight to afford **1-Nd** as green crystals (0.160 g, 15%). Anal calcd (%) for C₄₈H₈₈B₂Nd₂P₄: C, 52.41; H, 8.07. Found (%): C, 50.41; H, 8.07. μ_{eff} (Evans method, 298 K, C₆D₆): 4.02 μ_B. ¹H NMR (C₆D₆, 500 MHz, 298 K): δ = −13.86 (br, 8H, ν_{1/2} = 130 Hz, Htp-CH), −5.09 (br, 72H, ν_{1/2} = 150 Hz, C(CH₃)₃), BH₄ signals could not be observed. The paramagnetism of **1-Nd** precluded assignment of its ¹³C{¹H}, ¹¹B{¹H} and ³¹P{¹H} NMR spectra. FTIR (ATR, microcrystalline): $\tilde{\nu}$ = 2956 (br, m), 2870 (br, m), 1644 (m), 1513 (s), 1459 (s), 1365 (br, m), 1276 (br, m), 1247 (br, m), 1085 (s), 977 (s), 921 (w), 894 (br, s), 877 (br, s), 865 (br, s), 821 (w), 797 (m), 774 (m), 755 (m), 705 (s), 683 (s), 661 (s), 635 (s), 611 (s), 592 (m), 552 (m), 542 (w), 498 (w), 475 (m), 413 (s) cm^{−1}.

[Sm(Htp)₂(μ-BH₄)₂ (1-Sm). Di-*n*-butyl ether (20 mL) was added to a pre-cooled (−78 °C) Rotaflow tap-appended ampoule containing [Sm(BH₄)₃(THF)_{3.5}] (0.894 g, 2 mmol) and K(Htp) (0.937 g, 4 mmol). The reaction mixture was refluxed for 16 hours, allowed to settle and filtered. The solution was concentrated to 2 mL and stored at −25 °C overnight to afford **1-Sm** as orange crystals (0.077 g, 7%). Anal calcd (%) for C₄₈H₈₈B₂Sm₂P₄: C, 51.83; H, 7.98. Found (%): C, 51.17; H, 8.03. μ_{eff} (Evans method, 298 K, C₆D₆): 2.38 μ_B. ¹H NMR (C₆D₆, 400 MHz, 298 K): δ = −25.22 (br, 8H, ν_{1/2} ~ 800 Hz, BH₄), −0.54 (72H, ν_{1/2} = 12 Hz, C(CH₃)₃), 16.40 (br, 8H, ν_{1/2} = 90 Hz, Htp-CH). ¹¹B{¹H} NMR (C₆D₆, 128 MHz, 298 K): δ = −71.18 (BH₄). The paramagnetism of **1-Sm** precluded assignment of its ¹³C{¹H} and ³¹P{¹H} NMR spectra. FTIR (ATR, microcrystalline): $\tilde{\nu}$ = 2957 (s), 2900 (m), 2865 (m), 2447 (br, m, B-H str.), 2376 (br, w, B-H str.), 2225 (br, s, B-H str.), 1460 (s), 1416 (s), 1391 (s), 1359 (s), 1301 (m), 1248 (s), 1194 (s), 1167 (w), 1085 (br, s), 1065 (s), 1020 (w), 991 (s), 920 (s), 893 (w), 824(w), 799 (s), 759 (s), 721 (m), 694 (s), 661 (s), 611 (s), 591 (s), 517 (w), 464 (w), 435 (w) cm^{−1}.

[La(Htp)₂(μ-BH₄)₂(K)(DME)₂]₂ (2-La). Dimethoxyethane (20 mL) was added to a pre-cooled (−78 °C) Rotaflow tap-appended ampoule containing [La(BH₄)₃(THF)_{3.5}] (0.654 g, 1.5 mmol) and K(Htp) (0.703 g, 3.0 mmol). The reaction mixture was allowed to warm to room temperature and refluxed for 16 hours, allowed to settle and filtered. The solvent was removed *in vacuo* and toluene (20 mL) was added. The resultant suspension was allowed to settle for 3 hours and filtered. The solution was concentrated to 3 mL and stored at −25 °C to afford **2-La** as colourless crystals (0.185 g, 16%). Anal calcd (%) for C₆₄H₁₃₆B₄La₂K₂O₈P₄: C, 49.37; H, 8.81. Found (%): C, 48.44; H, 8.84. ¹H NMR (C₆D₆, 400 MHz, 298 K): δ = 1.50-1.75 (br, 72H, C(CH₃)₃), 3.08 (s, 24H, OCH₃), 3.12 (s, 16H, OCH₂), 7.20-7.40 (br, 8H, Htp-CH), BH₄ signals could not be observed. ¹¹B{¹H} NMR (C₆D₆, 128 MHz, 298 K): δ = −22.70 (BH₄), −20.98 (BH₄). ¹³C{¹H} NMR (C₆D₆, 100 MHz, 298 K): δ = 34.55 (d, ³J_{PC} = 6.9 Hz, C(CH₃)₃), 37.00 (d, ²J_{PC} = 15.7 Hz, C(CH₃)₃), Htp-C signals could not be observed. ³¹P{¹H} NMR (C₆D₆, 162 MHz, 298 K): δ = 96.49 (Htp-P). FTIR (ATR, microcrystalline): $\tilde{\nu}$ = 2946 (s), 2899 (m), 2868 (w), 2427 (s, B-H str.), 2224 (br, m, B-H str.), 2178 (br, m, B-H str.), 1458 (s), 1390 (s), 1363 (s), 1355 (s), 1235 (s), 1152 (s), 1075 (s), 1022 (s), 990 (m), 842 (s), 797 (s), 776 (s), 723 (s), 660 (s), 617 (s), 593 (s) cm^{−1}.

[Ce(Htp)₂(μ-BH₄)₂(K)(DME)₂]₂ (2-Ce). Dimethoxyethane (20 mL) was added to a pre-cooled (−78 °C) Rotaflow tap-appended ampoule containing [Ce(BH₄)₃(THF)_{3.5}] (0.655 g, 1.5 mmol) and K(Htp) (0.703 g, 3.0 mmol). The reaction mixture was allowed to warm to room temperature and refluxed for 16 hours, allowed to settle and filtered. The solvent was removed *in vacuo* and toluene (20 mL) was added. The resultant suspension was allowed to settle for 3 hours and filtered. The solution was concentrated to 3 mL and stored at −25 °C to afford **2-Ce** as yellow crystals (0.539 g, 46%). Anal calcd (%) for C₆₄H₁₃₆B₄Ce₂K₂O₈P₄: C, 49.30; H, 8.79. Found (%): C, 47.86; H, 8.61. μ_{eff} (Evans method, 298 K, C₆D₆): 3.52 μ_{B} . ¹H NMR (C₆D₆, 400 MHz, 298 K): δ = −3.68 (br, 48H, $\nu_{1/2}$ = 90 Hz, C(CH₃)₃), −1.84 (br, 24H, $\nu_{1/2}$ = 140 Hz, C(CH₃)₃), 3.54 (br, 40H, $\nu_{1/2}$ = 25 Hz, CH₂OCH₃), 11.35 (br, 8H, $\nu_{1/2}$ = 220 Hz, Htp-CH), BH₄ signals could not be observed. ¹¹B{¹H} NMR (C₆D₆, 128 MHz, 298 K): δ = 13.35 (BH₄). The paramagnetism of **2-Ce** precluded assignment of its ¹³C{¹H} and ³¹P{¹H} NMR spectra. FTIR (ATR, microcrystalline): $\tilde{\nu}$ = 2945 (s), 2899 (m), 2866 (w), 2828 (w), 2427 (s, B-H str.), 2225 (br, m,

B-H str.), 1457 (s), 1355 (s), 1234 (s), 1194 (s), 1153 (s), 1098 (s), 1076 (s), 1019 (s), 854 (s), 776 (s), 724 (s), 660 (s), 617 (s), 593 (s) cm^{-1} .

[Ce(Htp)₂(μ -BH₄)₂(K)(Et₂O)(THF)]_∞ (3-Ce): Diethyl ether (20 mL) was added to a Schlenk containing a pre-cooled (−78 °C) mixture of [Ce(BH₄)₃(THF)_{3.5}] (0.874 g, 2 mmol) and K(Htp) (0.937 g, 4 mmol). The reaction mixture was allowed to warm to room temperature and stirred for 16 hours, settled and filtered. The resultant yellow solution was concentrated to 3 mL and stored at −25 °C to afford **3-Ce** as orange crystals (0.456 g, 31%). Anal calcd (%) for C₂₄H₄₈B₂CeKP₂ (desolvated): C, 48.09; H, 8.07. Found (%): C, 48.03; H, 8.08. μ_{eff} (Evans method, 298 K, C₆D₆): 2.33 μ_{B} . ¹H NMR (C₆D₆, 500 MHz, 298 K): δ = −3.45 (br, 36H, $\nu_{1/2}$ = 250 Hz, C(CH₃)₃), 1.44 (br, 4H, $\nu_{1/2}$ = 120 Hz, Htp-CH), BH₄ signals could not be observed. The paramagnetism of **3-Ce** precluded assignment of its ¹³C{¹H}, ¹¹B{¹H} and ³¹P{¹H} NMR spectra. FTIR (ATR, microcrystalline): $\tilde{\nu}$ = 2957 (s), 2901 (m), 2866 (m), 2429 (br, w, B-H str.), 2373 (br, w, B-H str.), 2277 (s, B-H str.), 2214 (s, B-H str.), 1460 (s), 1391 (s), 1359 (s), 1248 (s), 1194 (s), 1163 (s), 1115 (s), 1038 (s), 1020 (m), 865 (br, m), 808 (s), 721 (s), 660 (s), 612 (s), 591 (s), 549 (w) cm^{-1} .

2. Crystallography

The crystal data for complexes **1-Ln** (Ln = La, **1-La**; Ce, **1-Ce**; Nd, **1-Nd**; Sm, **1-Sm**; **2-Ln** (Ln = La, **2-La**; Ce, **2-Ce**) and **3-Ce** are compiled in Tables S1-S3. Crystals of **1-Nd**, **2-Ce** and **3-Ce** were examined using an Oxford Diffraction Supernova diffractometer with a CCD area detector and a mirror-monochromated Mo K α radiation ($\lambda = 0.71073 \text{ \AA}$). Crystals of **1-La**, **1-Ce**, **1-Sm** and **2-La** were examined using a Rigaku XtalLAB AFC11 diffractometer with a CCD area detector and a graphite-monochromated Cu K α ($\lambda = 1.54178 \text{ \AA}$) or Mo K α radiation ($\lambda = 0.71073 \text{ \AA}$). Intensities were integrated from data recorded on 0.5° (**1-La**, **1-Ce**, **1-Sm**, **2-La**), 0.9° (**3-Ce**) or 1° (**1-Nd**, **2-Ce**) frames by ω rotation. Cell parameters were refined from the observed positions of all strong reflections in each data set. A Gaussian grid face-indexed (**1-La**, **1-Ce**, **1-Nd**, **1-Sm**, **2-La**, **2-Ce** or analytical (**3-Ce**) absorption correction with a beam profile was applied.¹ The structures were solved using SHELXS;² the datasets were refined by full-matrix least-squares on all unique F^2 values,³ with anisotropic displacement parameters for all non-hydrogen atoms, and with constrained riding hydrogen geometries; $U_{\text{iso}}(\text{H})$ was set at 1.2 (1.5 for methyl groups) times U_{eq} of the parent atom. The largest features in final difference syntheses were close to heavy atoms and were of no chemical significance. CrysAlisPro¹ was used for control and integration, and SHELX^{2,3} was employed through OLEX2⁴ for structure solution and refinement. ORTEP-3⁵ and POV-Ray⁶ were employed for molecular graphics. CCDC 1992248-1992254 contain the supplementary crystal data for this article. These data can be obtained free of charge from the Cambridge Crystallographic Data Centre via www.ccdc.cam.ac.uk/data_request/cif.

Table S1. Crystallographic data for **1-La** and **1-Ce**.

^aConventional $R = \Sigma||F_o| - |F_c||/\Sigma|F_o|$; $R_w = [\Sigma w(F_o^2 - F_c^2)^2/\Sigma w(F_o^2)^2]^{1/2}$; $S = [\Sigma w(F_o^2 - F_c^2)^2/\text{no. data} - \text{no. params}]^{1/2}$ for all data.

	1-La	1-Ce
Formula	C ₄₈ H ₈₈ B ₂ La ₂ P ₄	C ₄₈ H ₈₈ B ₂ Ce ₂ P ₄
Formula weight	1088.50	1090.92
Crystal size, mm	0.182 × 0.143 × 0.087	0.161 × 0.142 × 0.095
Crystal system	Monoclinic	Monoclinic
Space group	<i>I</i> 2/ <i>a</i>	<i>I</i> 2/ <i>a</i>
<i>a</i> , Å	20.7897(10)	20.647(3)
<i>b</i> , Å	12.9165(4)	12.9366(9)
<i>c</i> , Å	20.3007(6)	20.2887(17)
α , °	90	90
β , °	92.015(4)	91.935(10)
γ , °	90	90
<i>V</i> , Å ³	5448.0(4)	5416.1(9)
<i>Z</i>	4	4
ρ_{calc} , g cm ³	1.327	1.338
μ , mm ⁻¹	13.258	14.134
F(000)	2240	2248
No. of reflections (unique)	15175 (4809)	23912 (4950)
S ^a	1.06	1.07
$R_1(wR_2)$ ($F^2 > 2\sigma(F^2)$)	0.0982 (0.2536)	0.0925 (0.2215)
R_{int}	0.054	0.121
Min./max. diff map, Å ⁻³	-1.44, 4.01	-0.94, 2.46

Table S2. Crystallographic data for **1-Nd** and **1-Sm**.

^aConventional $R = \Sigma||F_o| - |F_c||/\Sigma|F_o|$; $R_w = [\Sigma w(F_o^2 - F_c^2)^2/\Sigma w(F_o^2)^2]^{1/2}$; $S = [\Sigma w(F_o^2 - F_c^2)^2/\text{no. data} - \text{no. params}]^{1/2}$ for all data.

	1-Nd	1-Sm
Formula	C ₄₈ H ₈₈ B ₂ P ₄ Nd ₂	C ₄₈ H ₈₈ B ₂ P ₄ Sm ₂
Formula weight	1099.16	1111.38
Crystal size, mm	0.272 × 0.224 × 0.103	0.14 × 0.118 × 0.086
Crystal system	Monoclinic	Monoclinic
Space group	<i>I</i> 2/ <i>a</i>	<i>I</i> 2/ <i>a</i>
a, Å	20.3618(13)	20.4242(11)
b, Å	12.8239(19)	12.8734(9)
c, Å	20.685(3)	20.6935(18)
α, °	90	90
β, °	93.734(10)	94.177(7)
γ, °	90	90
V, Å ³	5389.7(12)	5426.5(7)
Z	4	4
ρ _{calc} , g cm ³	1.355	1.360
μ, mm ⁻¹	2.053	17.394
F(000)	2240	2256
No. of reflections (unique)	8100 (4714)	13541 (4784)
S ^a	0.99	1.04
R ₁ (wR ₂) (F ² > 2σ(F ²))	0.1188 (0.2827)	0.0809 (0.2104)
R _{int}	0.183	0.094
Min./max. diff map, Å ⁻³	-1.69, 3.54	-1.16, 1.82

Table S3. Crystallographic data for **2-La**, **2-Ce** and **3-Ce**.

^aConventional $R = \Sigma||Fo| - |Fc||/\Sigma|Fo|$; $Rw = [\Sigma w(Fo^2 - Fc^2)^2/\Sigma w(Fo^2)^2]^{1/2}$; $S = [\Sigma w(Fo^2 - Fc^2)^2/\text{no. data} - \text{no. params}]^{1/2}$ for all data.

	2-La	2-Ce	3-Ce
Formula	C ₆₄ H ₁₃₆ B ₄ K ₂ La ₂ O ₈ P ₄	C ₆₄ H ₁₃₆ B ₄ Ce ₂ K ₂ O ₈ P ₄	C ₃₂ H ₆₄ B ₂ KCeO ₂ P ₂
Formula weight	1556.86	1559.28	745.62
Crystal size, mm	0.272 × 0.258 × 0.226	0.504 × 0.204 × 0.171	0.285 × 0.148 × 0.100
Crystal system	Monoclinic	Monoclinic	Monoclinic
Space group	<i>P2₁/n</i>	<i>P2₁/n</i>	<i>P2₁/c</i>
a, Å	10.6790(2)	10.6463(4)	19.8610(10)
b, Å	21.0788(4)	21.0099(9)	15.8524(6)
c, Å	18.7550(5)	18.7079(8)	12.8759(7)
α, °	90	90	90
β, °	98.041(2)	98.442(4)	106.613(5)
γ, °	90	90	90
V, Å ³	4180.24(17)	4139.2(3)	3884.7(3)
Z	2	2	4
ρ _{calc} , g cm ³	1.237	1.251	1.275
μ, mm ⁻¹	1.227	1.307	1.386
F(000)	1631	1636	1556
No. of reflections (unique)	40661 (7657)	19886 (7572)	22301 (7108)
S ^a	1.05	1.02	1.02
R ₁ (wR ₂) (F ² > 2σ(F ²))	0.0278 (0.0579)	0.0475 (0.0772)	0.0464 (0.0767)
R _{int}	0.063	0.060	0.071
Min./max. diff map, Å ⁻³	-0.39, 0.47	-0.51, 0.72	-0.54, 1.33

3. Molecular structures of complexes 1-La, 1-Ce, 1-Nd and 1-Sm

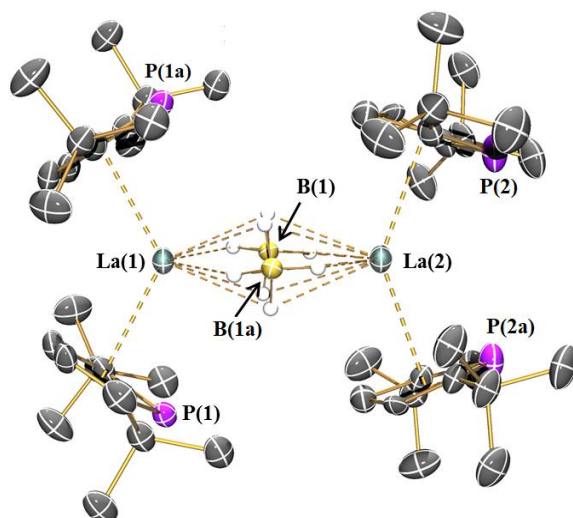


Figure S1. Molecular structure of $[\text{La}(\text{Htp})_2(\mu\text{-BH}_4)_2]$ (**1-La**) with selected labelling. Displacement ellipsoids set at 30% probability level and hydrogen atoms apart from those on BH_4^- anions are omitted for clarity. Selected distances and angles: $\text{La1}\cdots(\text{Htp})_{\text{centroid1}}$, 2.634(7) Å; $\text{La2}\cdots(\text{Htp})_{\text{centroid2}}$, 2.664(6) Å; $\text{La1}\cdots\text{B1}$, 2.855(13) Å; $\text{La2}\cdots\text{B1}$, 2.914(13) Å; $(\text{Htp})_{\text{centroid1}}\cdots\text{La1}\cdots(\text{Htp})_{\text{centroid1a}}$, 123.7(2)°; $(\text{Htp})_{\text{centroid1}}\cdots\text{La1}\cdots(\text{Htp})_{\text{centroid1a}}$, 141.0(2)°.

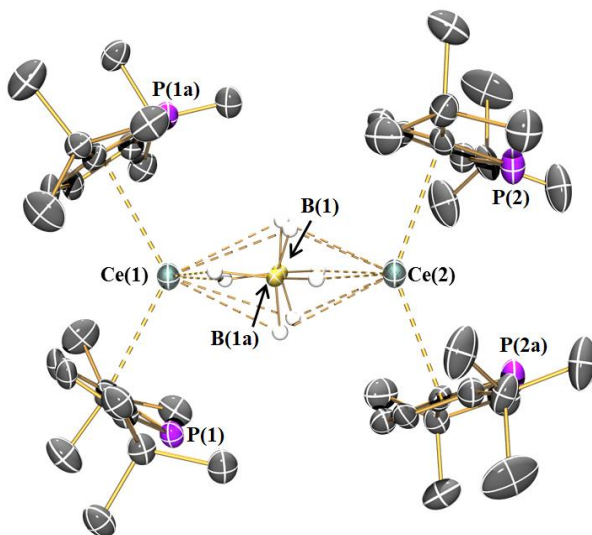


Figure S2. Molecular structure of $[\text{Ce}(\text{Htp})_2(\mu\text{-BH}_4)_2]$ (**1-Ce**) with selected labelling. Displacement ellipsoids set at 30% probability level and hydrogen atoms apart from those on BH_4^- anions are omitted for clarity. Selected distances and angles: $\text{Ce1}\cdots(\text{Htp})_{\text{centroid1}}$, 2.605(6) Å; $\text{Ce2}\cdots(\text{Htp})_{\text{centroid2}}$, 2.626(6) Å; $\text{Ce1}\cdots\text{B1}$, 2.904(12) Å; $\text{Ce2}\cdots\text{B1}$, 3.009(12) Å; $(\text{Htp})_{\text{centroid1}}\cdots\text{Ce1}\cdots(\text{Htp})_{\text{centroid1a}}$, 123.5(2)°; $(\text{Htp})_{\text{centroid2}}\cdots\text{Ce2}\cdots(\text{Htp})_{\text{centroid2a}}$, 140.1(2)°.

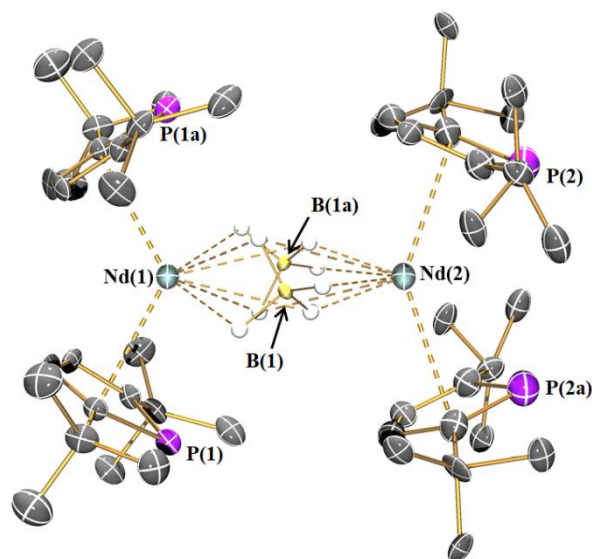


Figure S3. Molecular structure of $[\text{Nd}(\text{Htp})_2(\mu\text{-BH}_4)]_2$ (**1-Nd**) with selected labelling. Displacement ellipsoids set at 30% probability level and hydrogen atoms apart from those on BH_4^- anions are omitted for clarity. Crystallographic data quality only sufficient to demonstrate connectivity of the molecule.

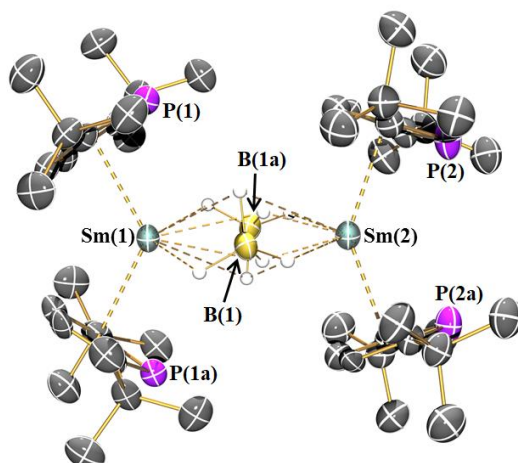


Figure S4. Molecular structure of $[\text{Sm}(\text{Htp})_2(\mu\text{-BH}_4)]_2$ (**1-Sm**) with selected labelling. Displacement ellipsoids set at 30% probability level and hydrogen atoms apart from those on BH_4^- anions are omitted for clarity. Selected distances and angles: $\text{Sm}1 \cdots (\text{Htp})_{\text{centroid}1}$, 2.544(6) Å; $\text{Sm}2 \cdots (\text{Htp})_{\text{centroid}2}$, 2.578(7) Å; $\text{Sm}1 \cdots \text{B}1$, 2.806(16) Å; $\text{Sm}2 \cdots \text{B}1$, 2.939(16) Å; $(\text{Htp})_{\text{centroid}1} \cdots \text{Sm}1 \cdots (\text{Htp})_{\text{centroid}1a}$, 124.7(2)°; $(\text{Htp})_{\text{centroid}2} \cdots \text{Sm}2 \cdots (\text{Htp})_{\text{centroid}2a}$, 141.8(2)°.

4. Molecular structures of complexes 2-La, 2-Ce and 3-Ce

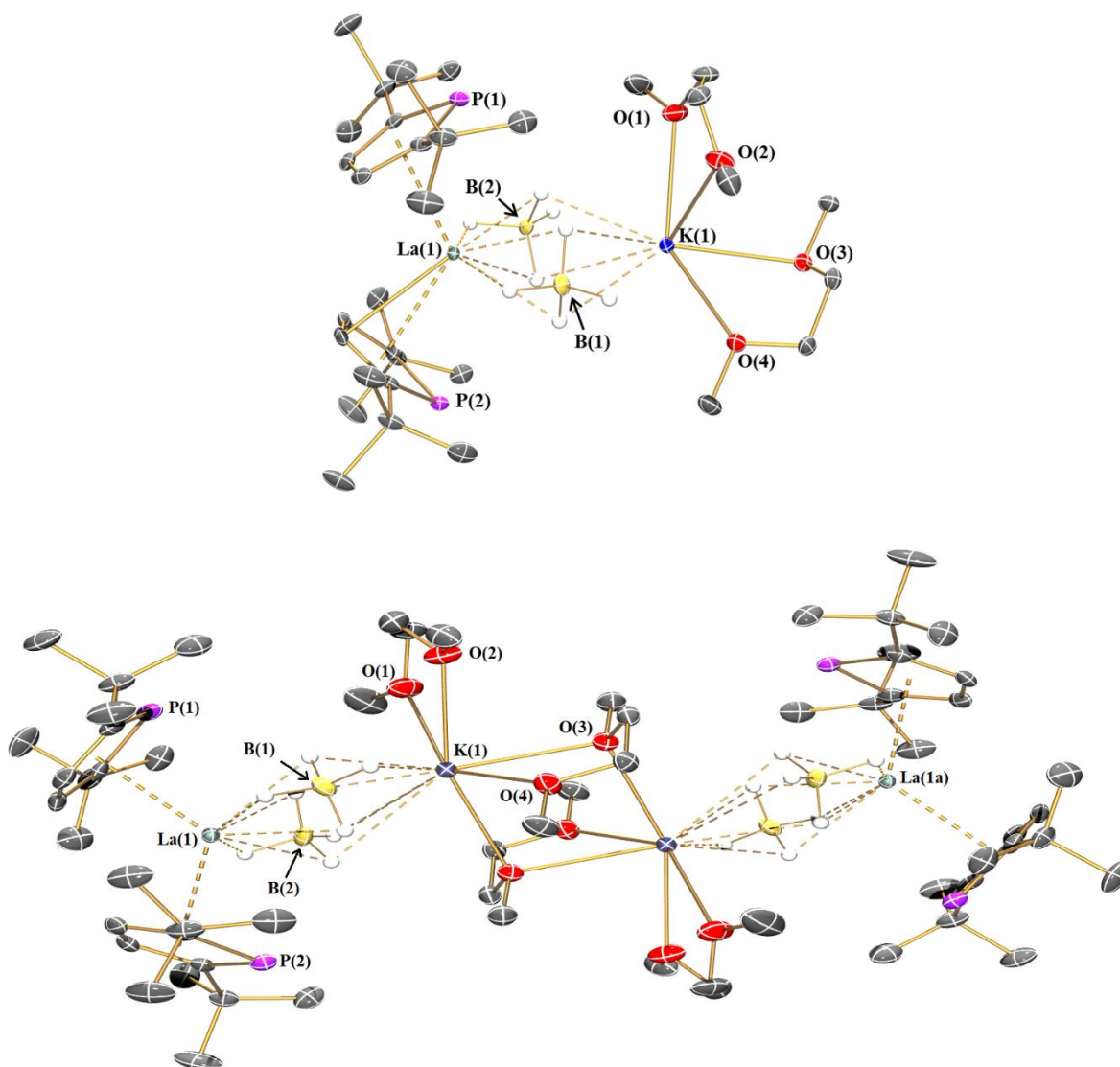


Figure S5. Molecular structure of $[\{\text{La}(\text{Htp})_2(\mu\text{-BH}_4)_2(\text{K})(\text{DME})_2\}_2]$ (**2-La**) with selected labelling. Displacement ellipsoids set at 30% probability level and hydrogen atoms apart from those on BH_4^- anions are omitted for clarity. Selected distances and angles: $\text{La}1\cdots(\text{Htp})_{\text{centroid}1}$, 2.6721(11) Å; $\text{La}1\cdots(\text{Htp})_{\text{centroid}2}$, 2.6672(11) Å; $\text{La}1\cdots\text{B}1$, 2.723(4) Å; $\text{La}1\cdots\text{B}2$, 2.724(3) Å; $(\text{Htp})_{\text{centroid}1}\cdots\text{La}1\cdots(\text{Htp})_{\text{centroid}2}$, 121.23(3)°.

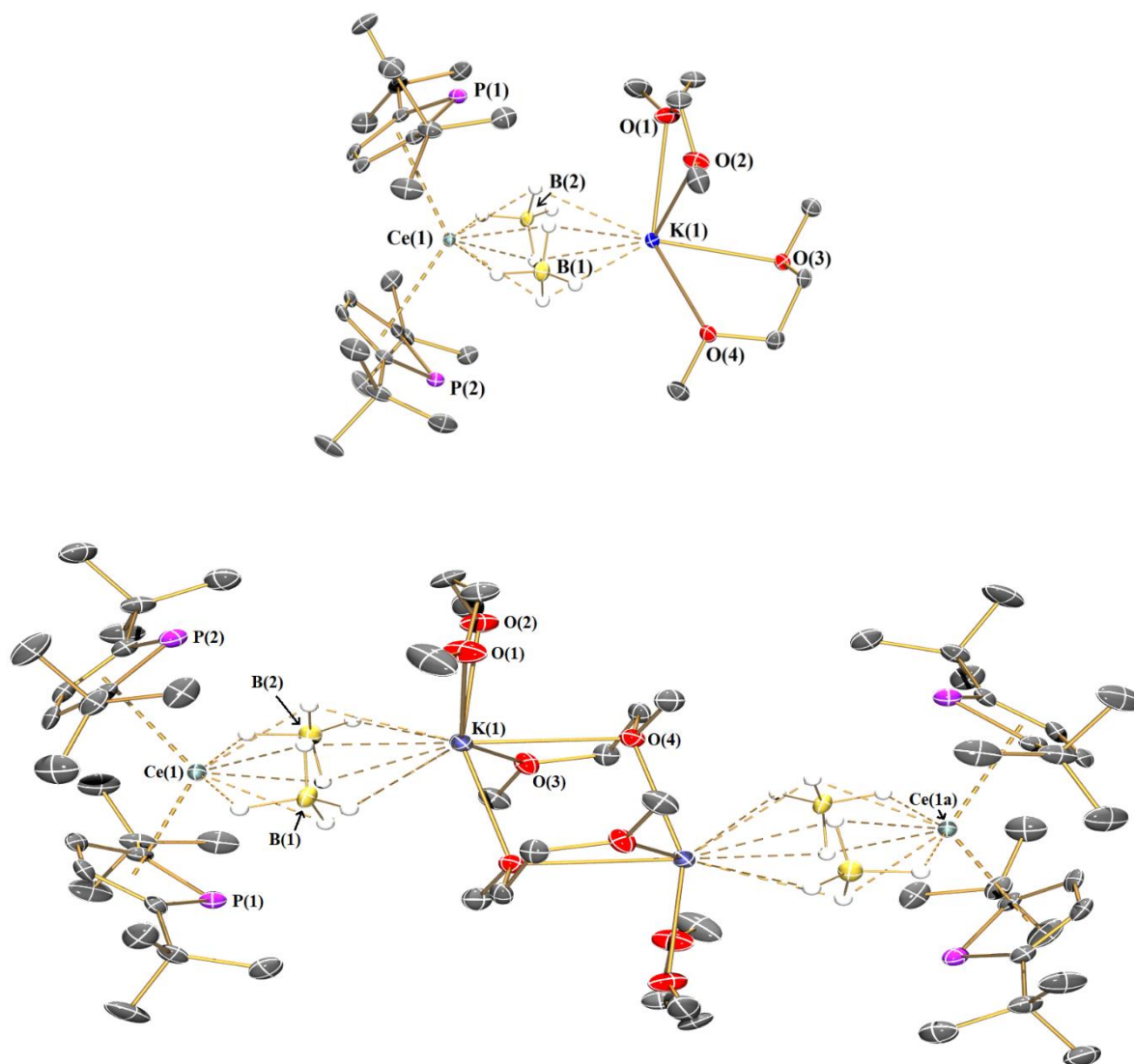


Figure S6. Molecular structure of $[\{Ce(Htp)_2(\mu-BH_4)_2(K)(DME)_2\}_2]$ (**2-Ce**) with selected labelling. Displacement ellipsoids set at 30% probability level and hydrogen atoms apart from those on BH_4^- anions are omitted for clarity. Selected distances and angles: $Ce1 \cdots (Htp)_{centroid1}$, 2.6288(18) Å; $Ce1 \cdots (Htp)_{centroid2}$, 2.6337(18) Å; $Ce1 \cdots B1$, 2.698(5) Å; $Ce1 \cdots B2$, 2.699(6) Å; $(Htp)_{centroid1} \cdots Ce1 \cdots (Htp)_{centroid2}$, 121.63(6)°.

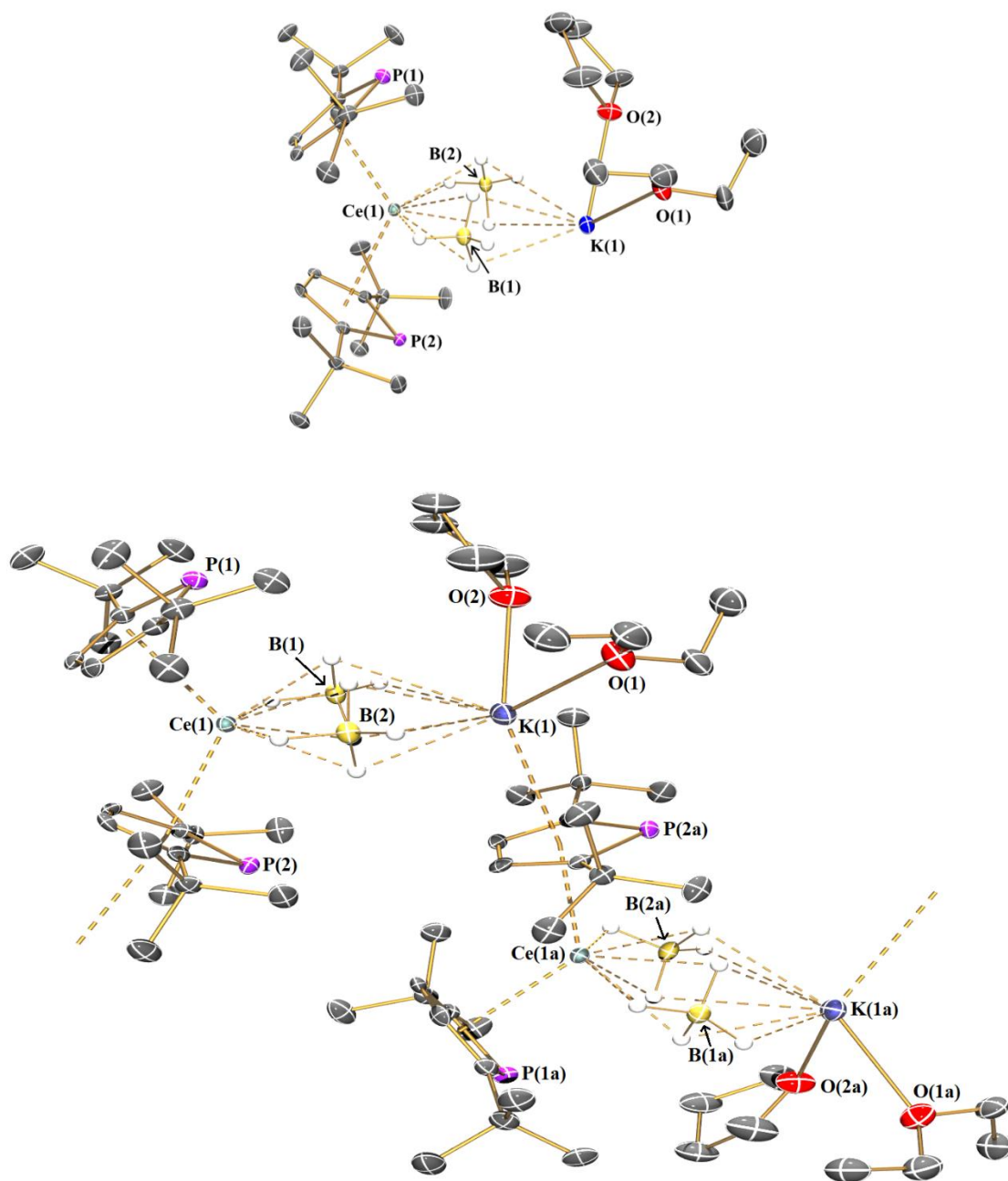


Figure S7. Molecular structure of $[\text{Ce}(\text{Htp})_2(\mu\text{-BH}_4)_2(\text{K})(\text{Et}_2\text{O})(\text{THF})]$ (**3-Ce**) with selected labelling. Displacement ellipsoids set at 30% probability level and hydrogen atoms apart from those on BH_4^- anions are omitted for clarity. Selected distances and angles: $\text{Ce1}\cdots(\text{Htp})_{\text{centroid1}}$, 2.632(2) Å; $\text{Ce1}\cdots(\text{Htp})_{\text{centroid2}}$, 2.683(2) Å; $\text{Ce1}\cdots\text{B1}$, 2.705(7) Å; $\text{Ce1}\cdots\text{B2}$, 2.695(5) Å; $(\text{Htp})_{\text{centroid1}}\cdots\text{Ce1}\cdots(\text{Htp})_{\text{centroid2}}$, 121.40(7)°.

5. NMR spectroscopy

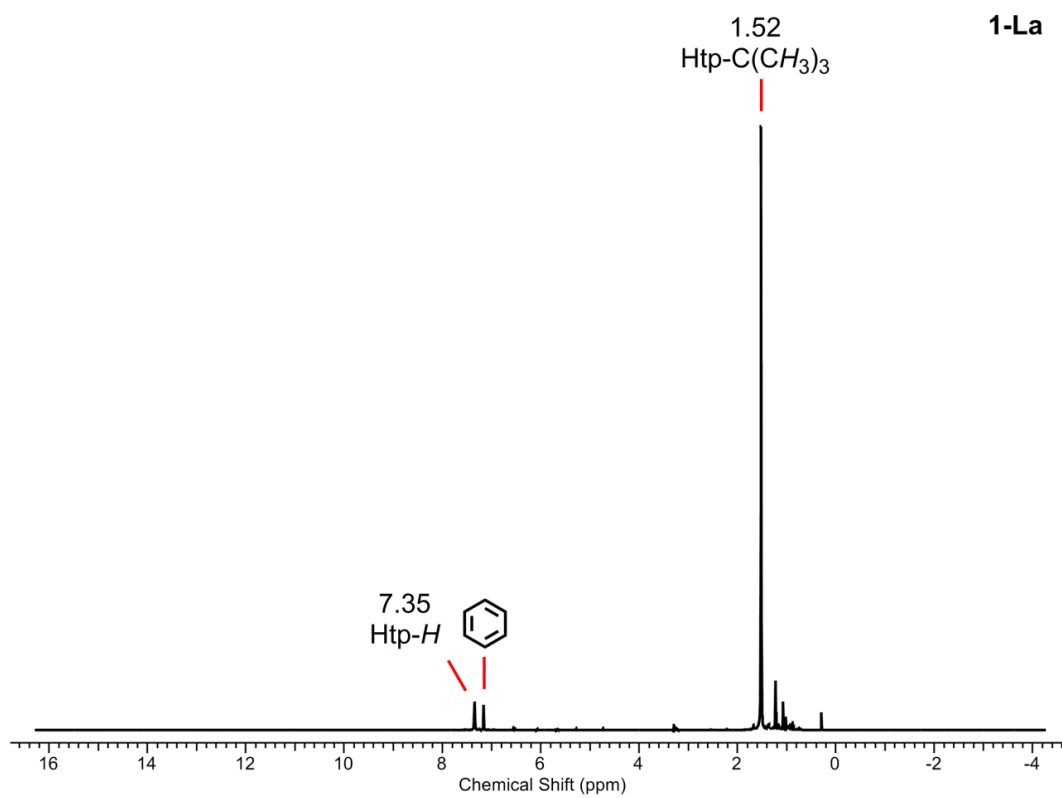


Figure S8. ¹H NMR spectrum of **1-La** in C₆D₆. Solvent residual marked.

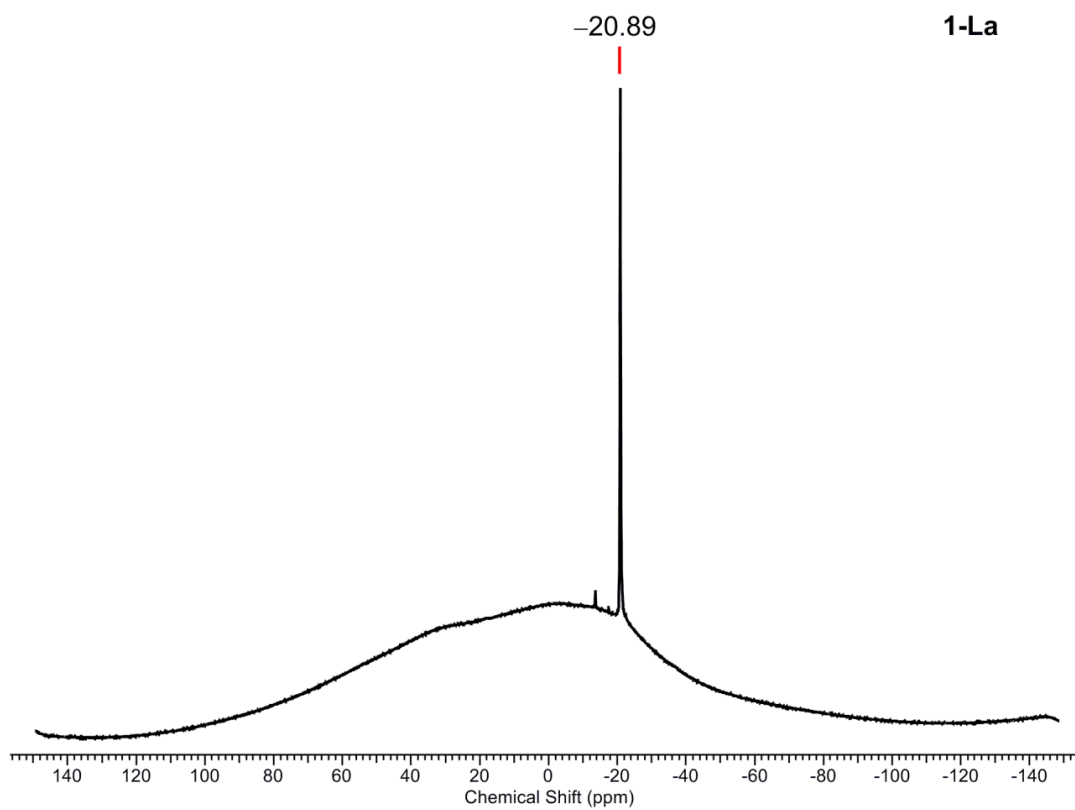


Figure S9. ¹¹B{¹H} NMR spectrum of **1-La** in C₆D₆.

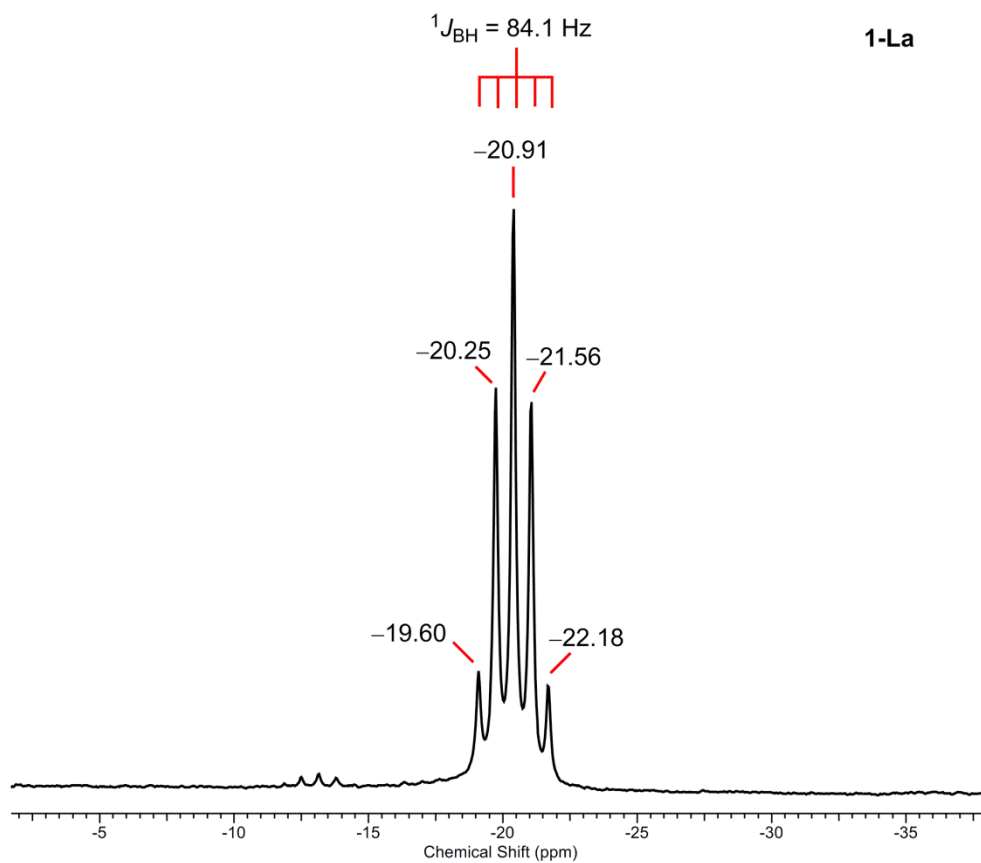


Figure S10. ^{11}B NMR spectrum of **1-La** in C_6D_6 .

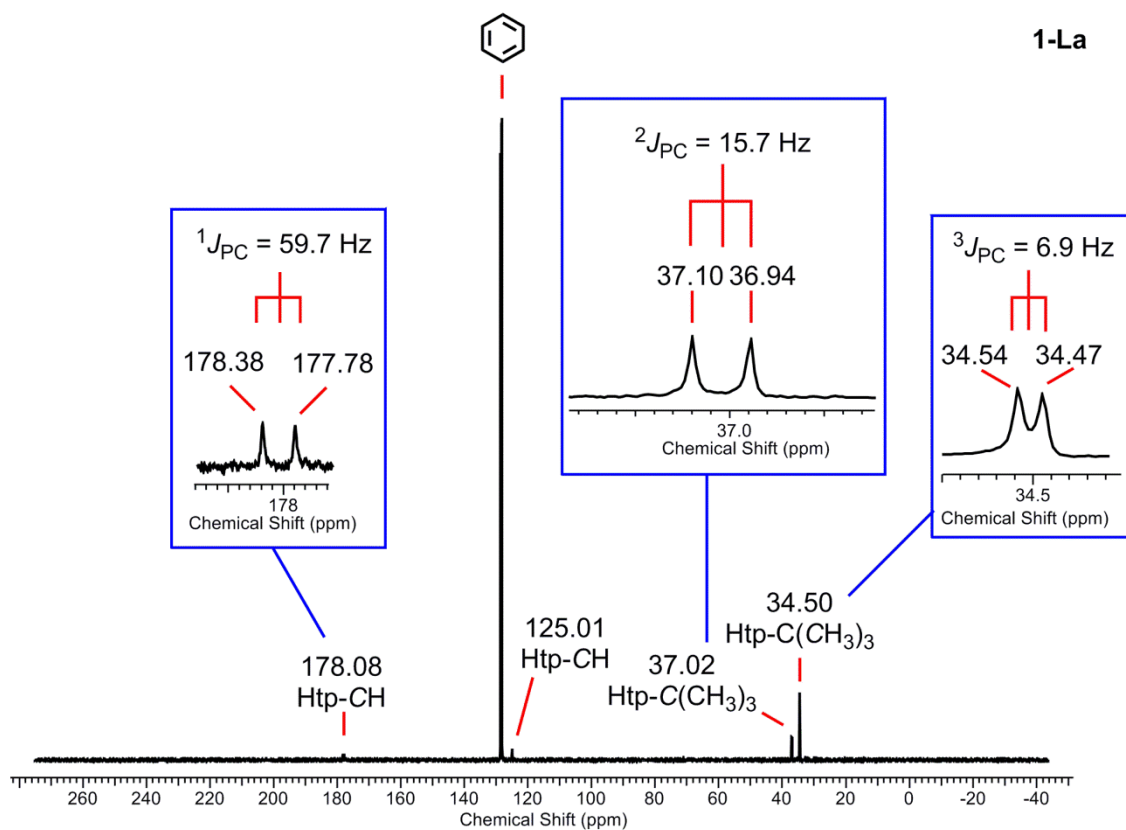


Figure S11. $^{13}\text{C}\{^1\text{H}\}$ NMR spectrum of **1-La** in C_6D_6 . Solvent residual marked.

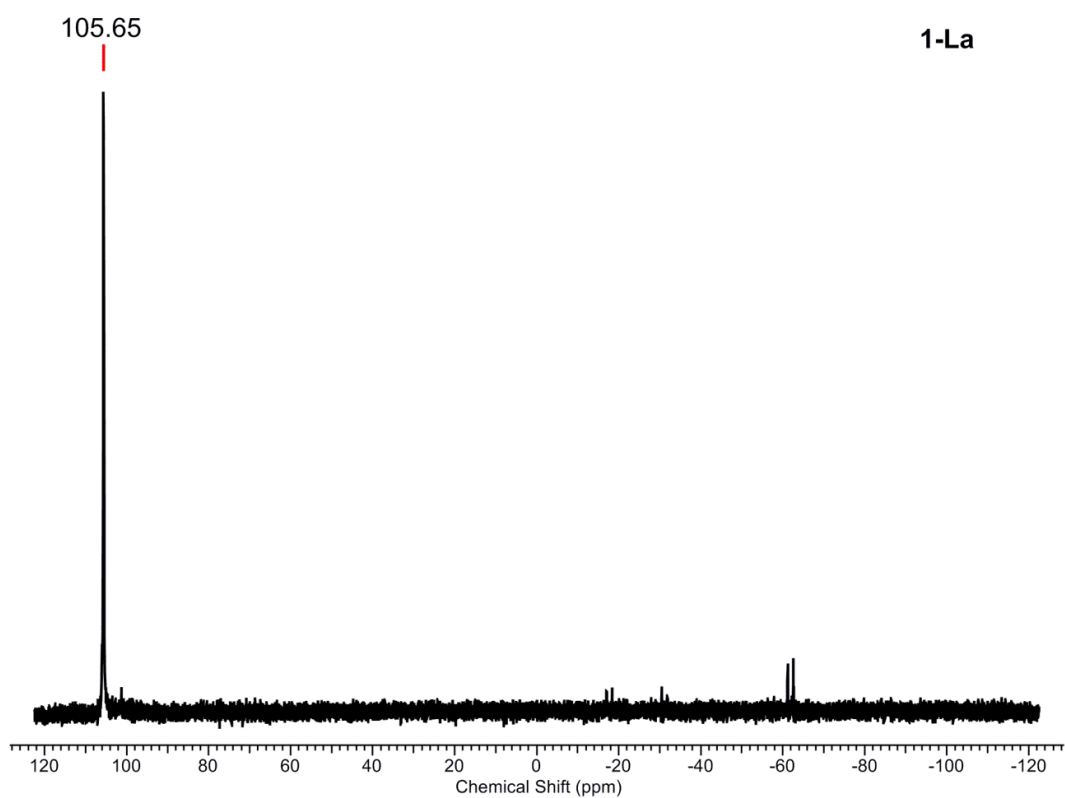


Figure S12. $^{31}\text{P}\{^1\text{H}\}$ NMR spectrum of **1-La** in C_6D_6 .

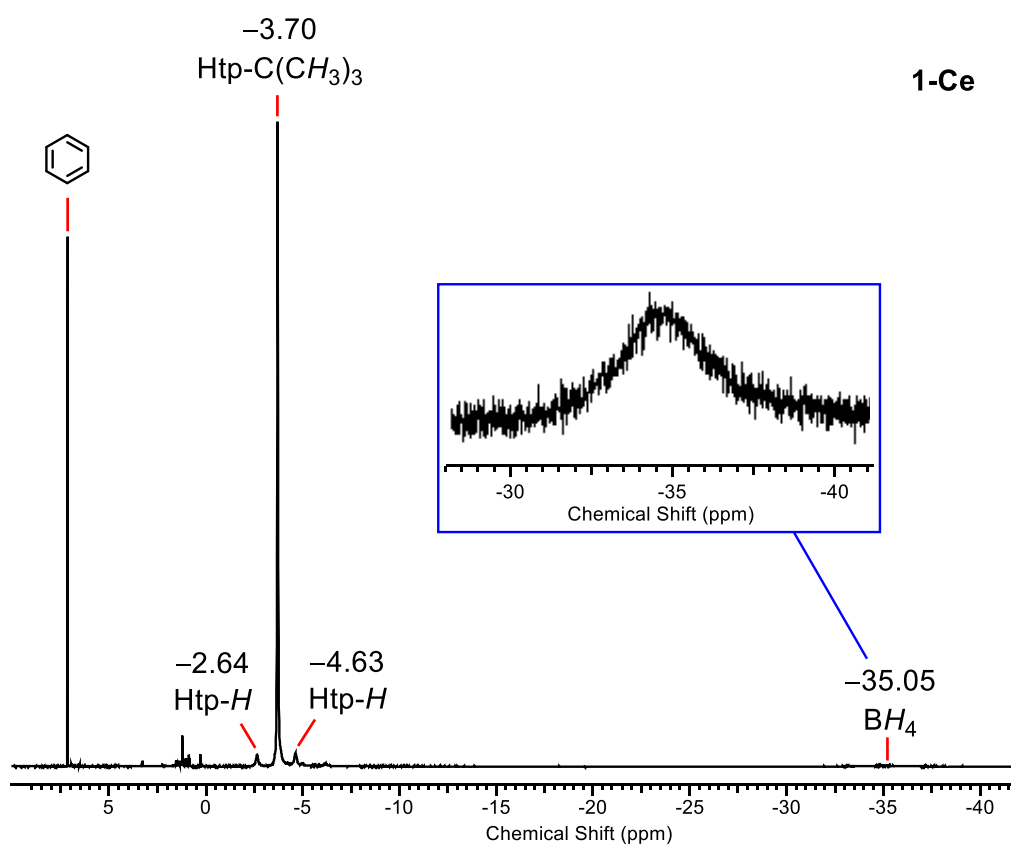


Figure S13. ^1H NMR spectrum of **1-Ce** in C_6D_6 in the region -40 to 12 ppm. Solvent residual marked.

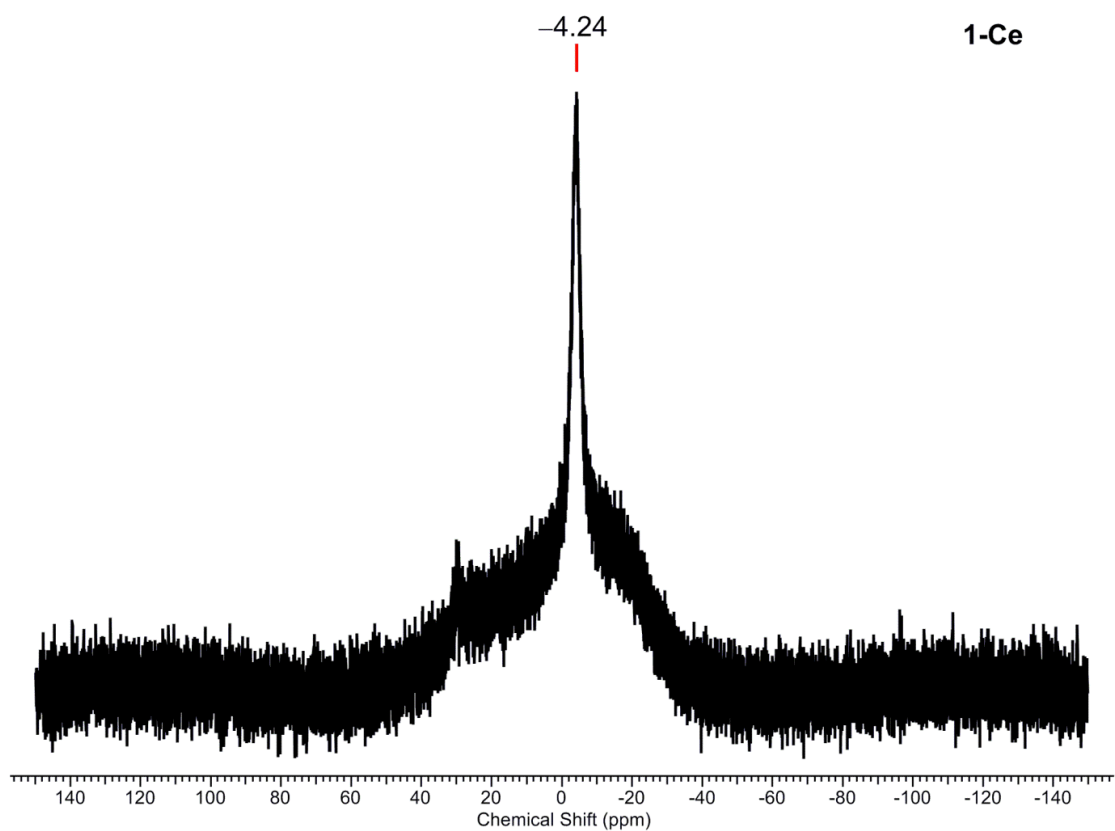


Figure S14. ^{11}B NMR spectrum of **1-Ce** in C_6D_6 .

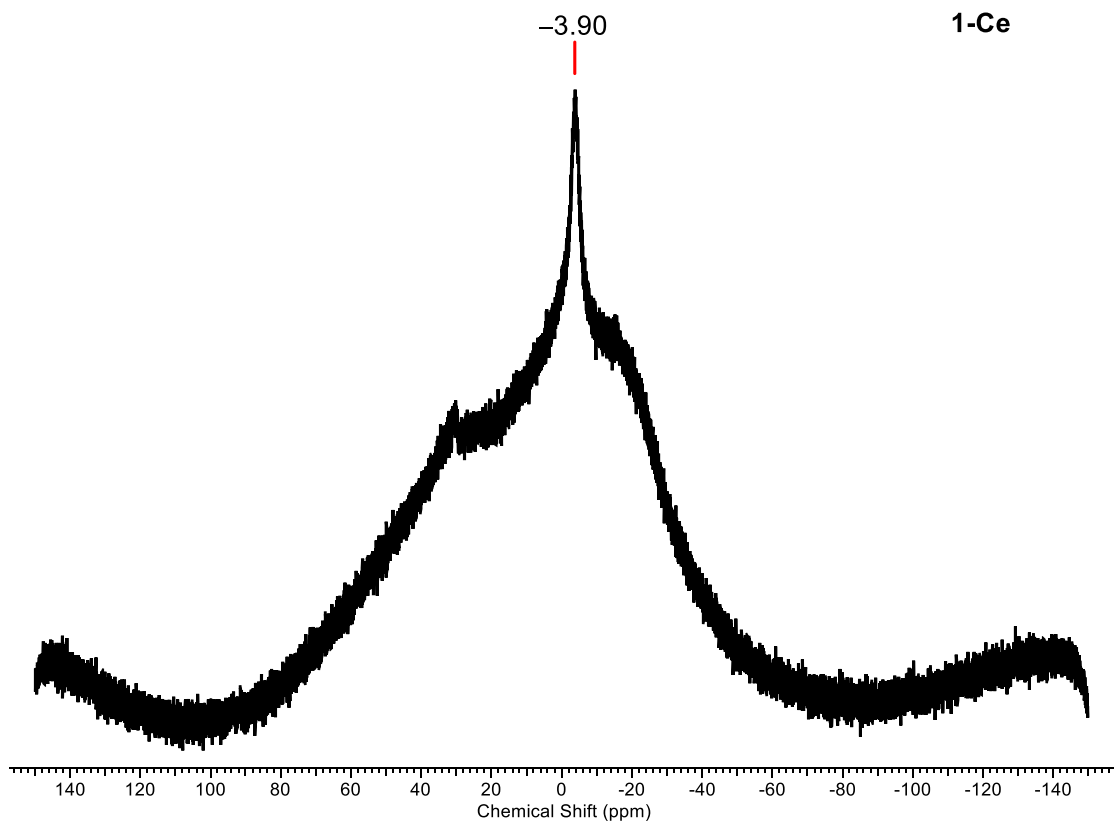


Figure S15. $^{11}\text{B}\{^1\text{H}\}$ NMR spectrum of **1-Ce** in C_6D_6 .

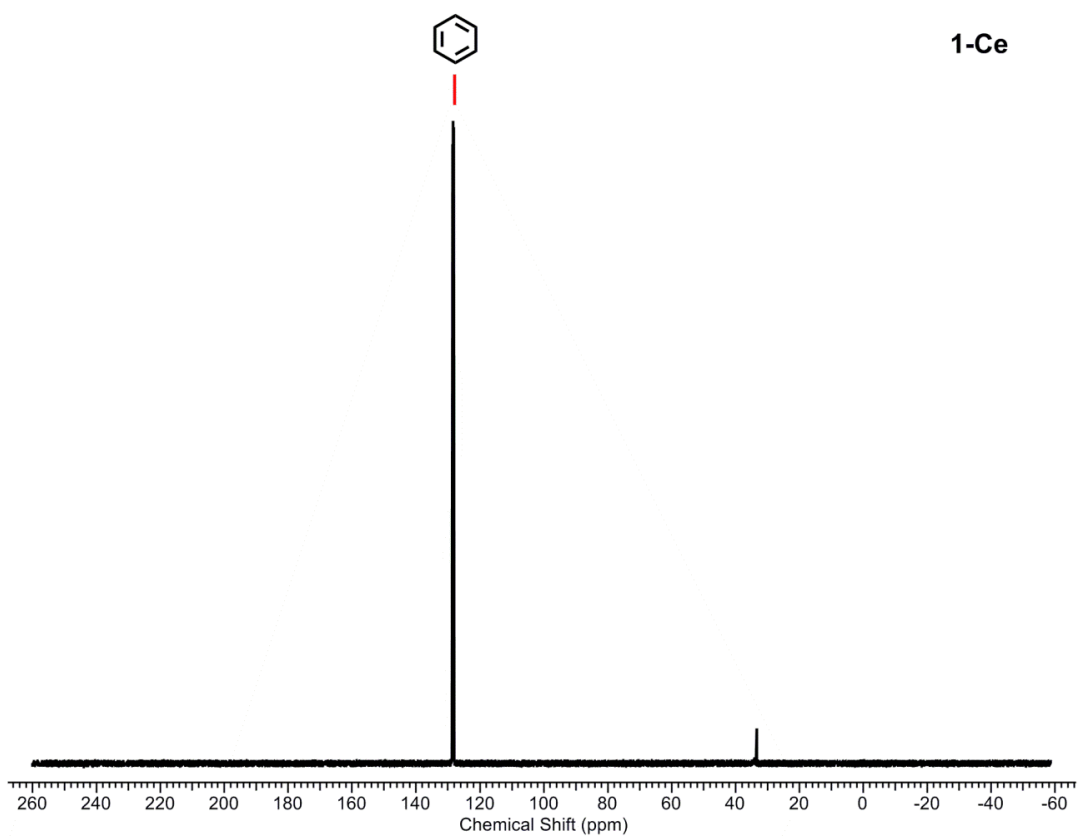


Figure S16. $^{13}\text{C}\{^1\text{H}\}$ NMR spectrum of **1-Ce** in C_6D_6 . Solvent residual marked.

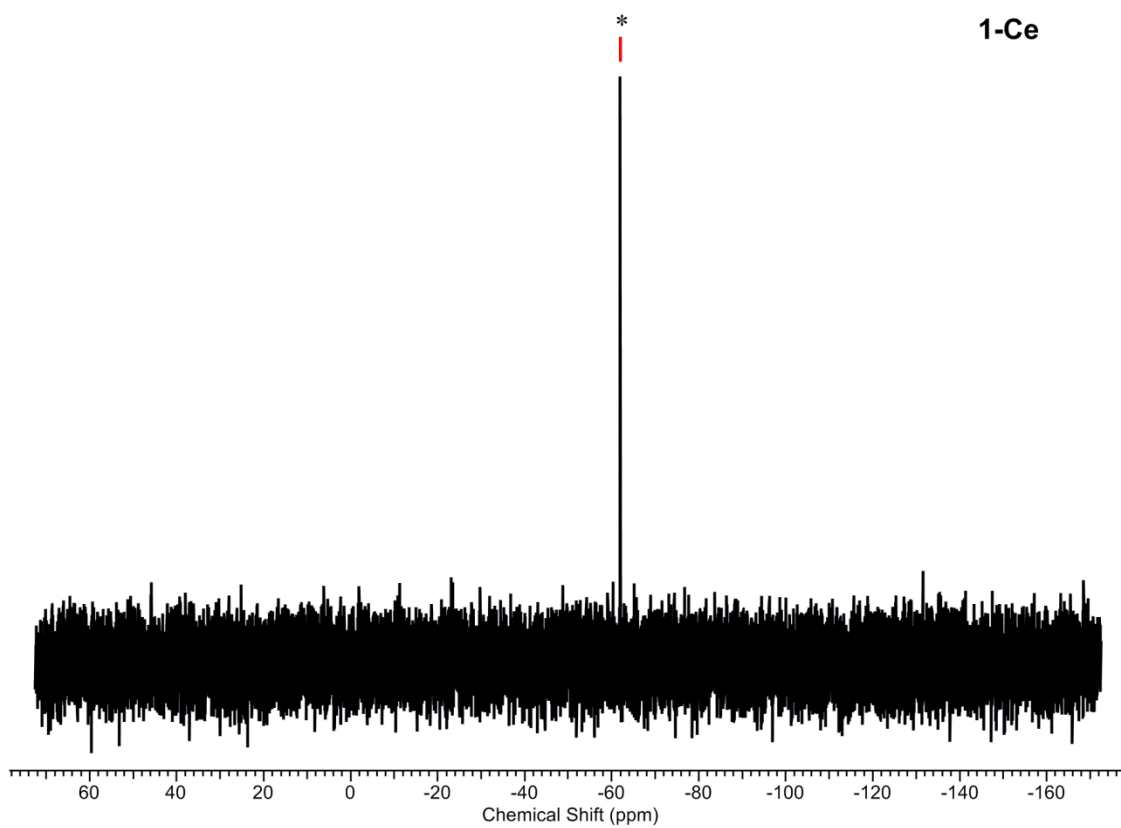


Figure S17. $^{31}\text{P}\{^1\text{H}\}$ NMR spectrum of **1-Ce** in C_6D_6 . * denotes diamagnetic impurities.

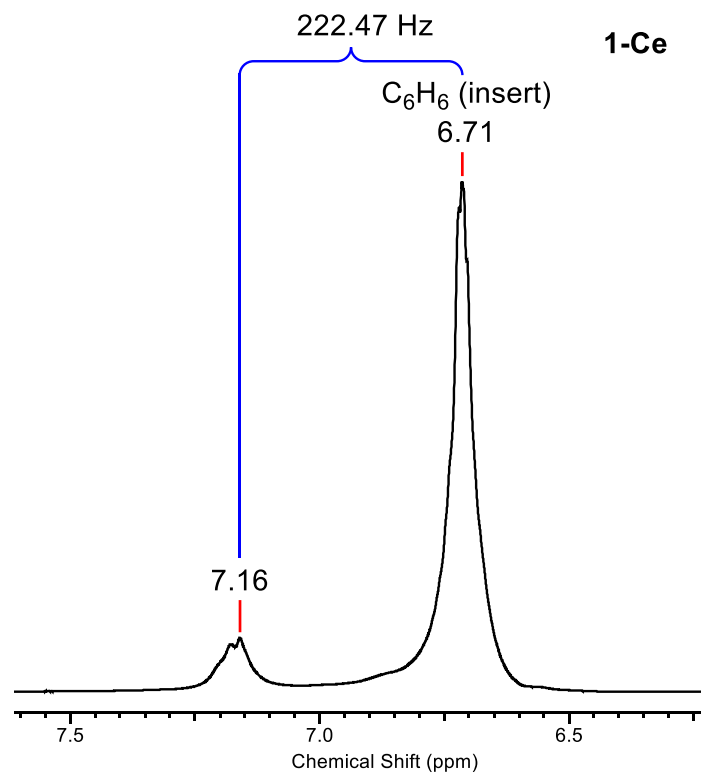


Figure S18. 1H NMR spectrum of **1-Ce** in C_6D_6 with a C_6H_6/C_6D_6 insert. Solvent residual marked.

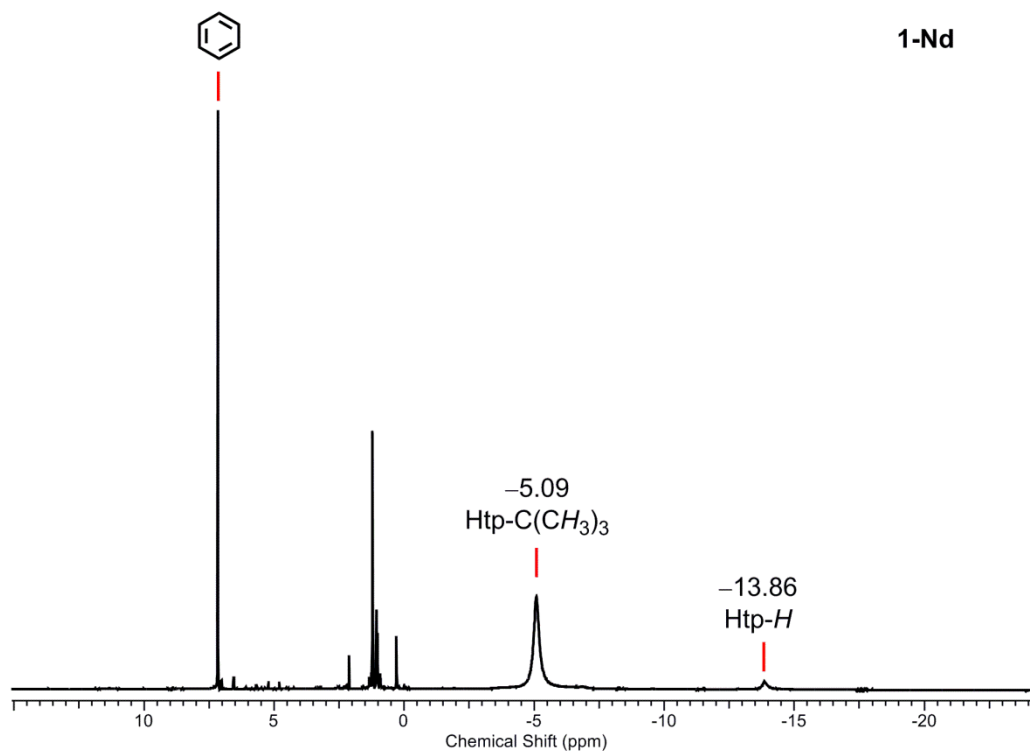


Figure S19. 1H NMR spectrum of **1-Nd** in C_6D_6 zoomed in the region -24 to 14 ppm. Solvent residual marked.

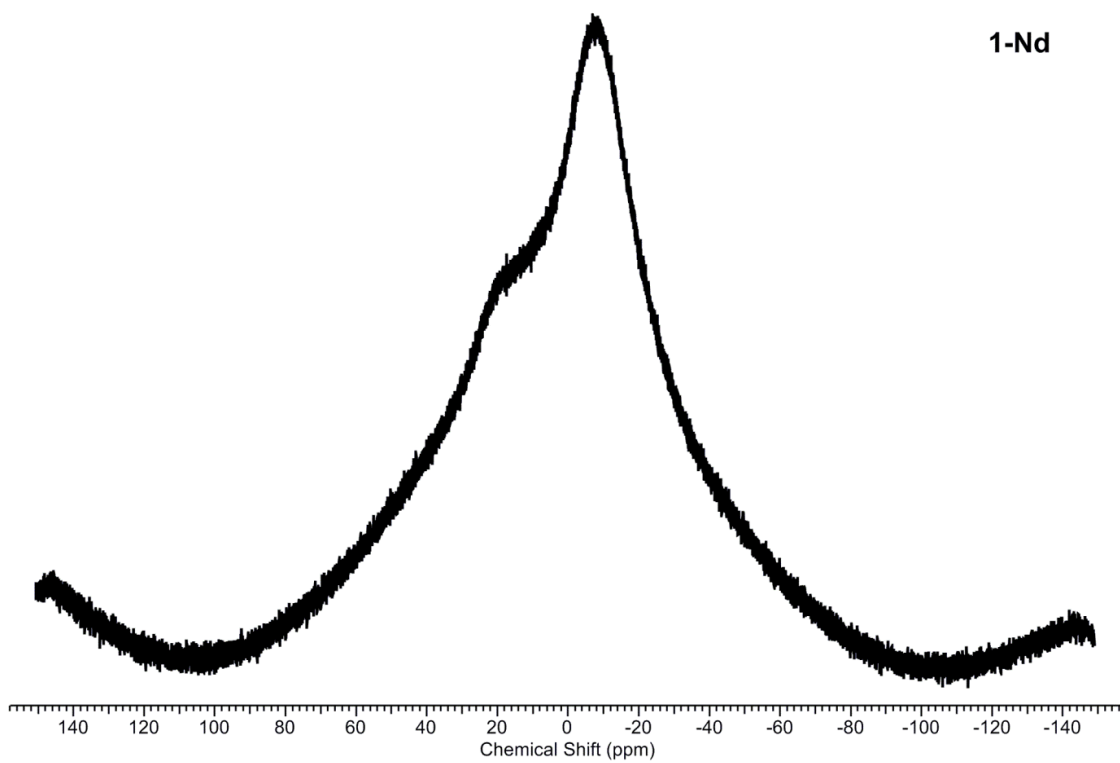


Figure S20. $^{11}\text{B}\{^1\text{H}\}$ NMR spectrum of **1-Nd** in C_6D_6 .

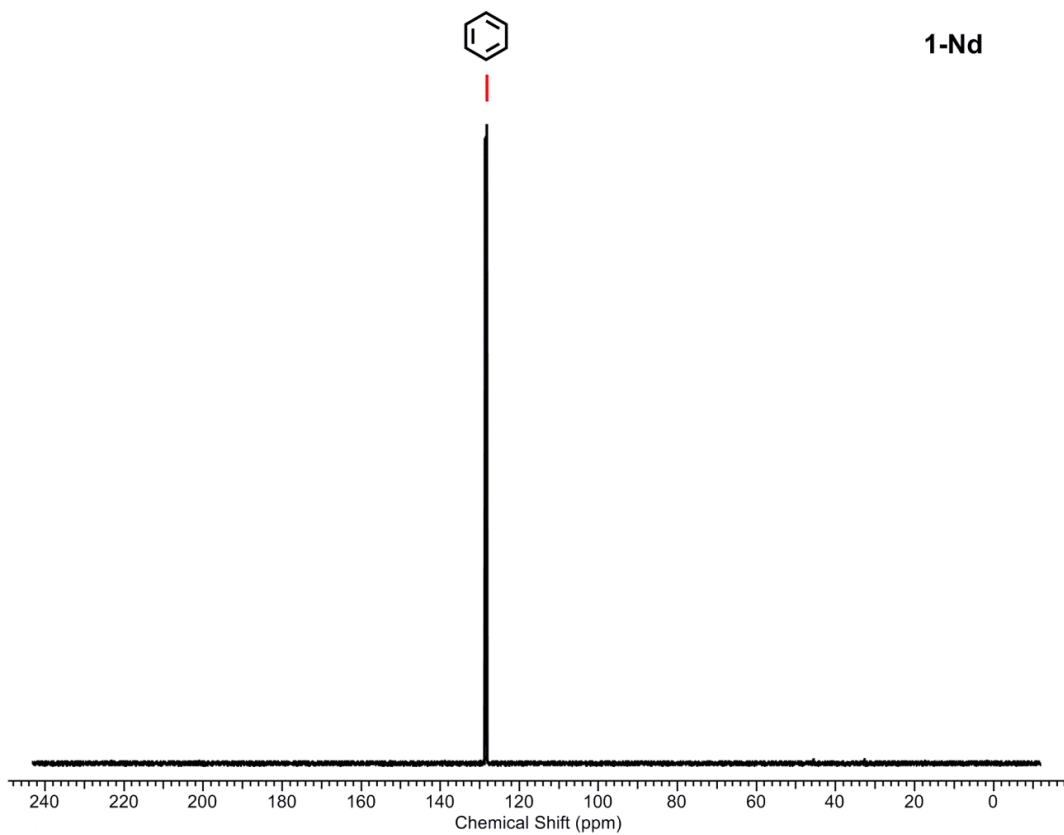


Figure S21. $^{13}\text{C}\{^1\text{H}\}$ NMR spectrum of **1-Nd** in C_6D_6 . Solvent residual marked.

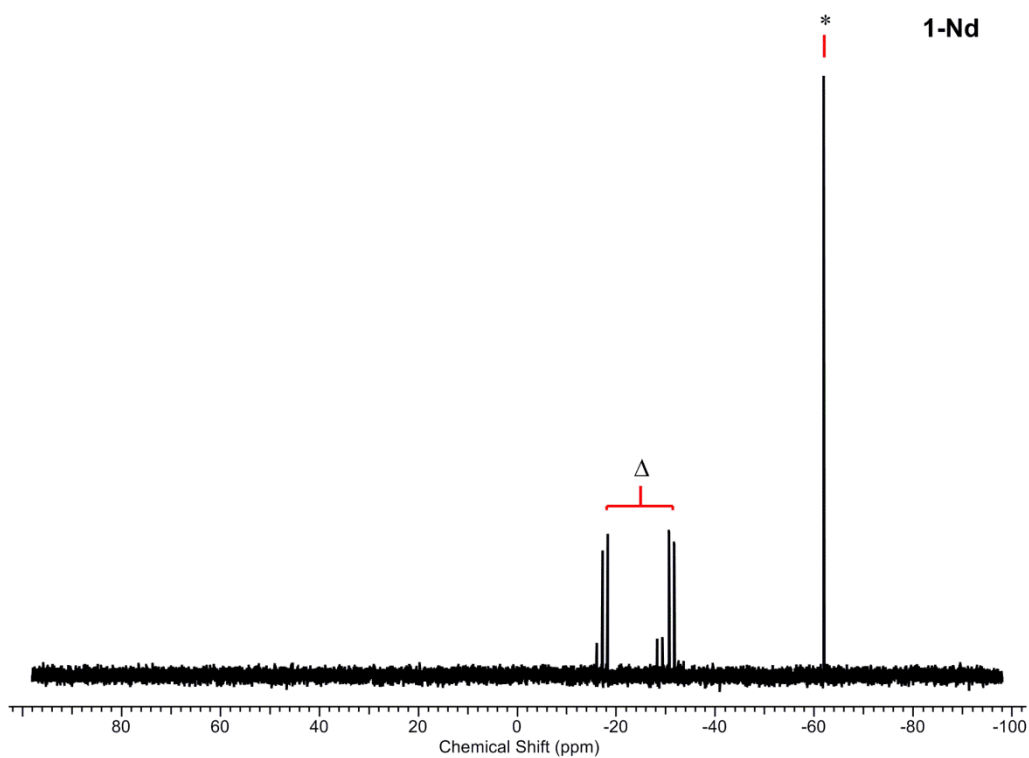


Figure S22. $^{31}\text{P}\{^1\text{H}\}$ NMR spectrum of **1-Nd** in C_6D_6 . * denotes diamagnetic impurities. Δ denotes $(\text{Htp})_2$ impurities.

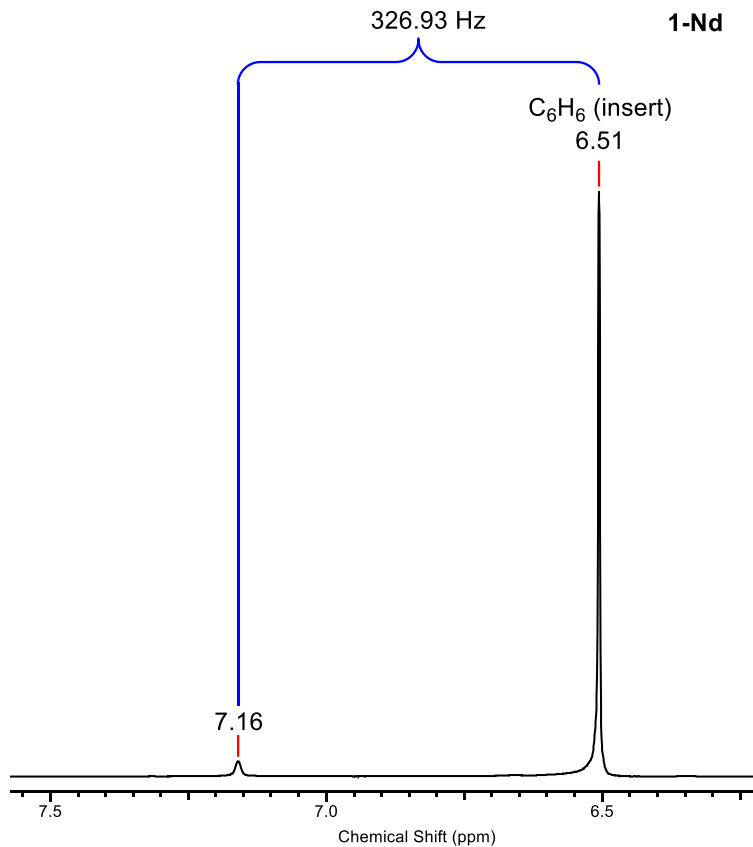


Figure S23. ^1H NMR spectrum of **1-Nd** in C_6D_6 with a $\text{C}_6\text{H}_6/\text{C}_6\text{D}_6$ insert. Solvent residual marked.

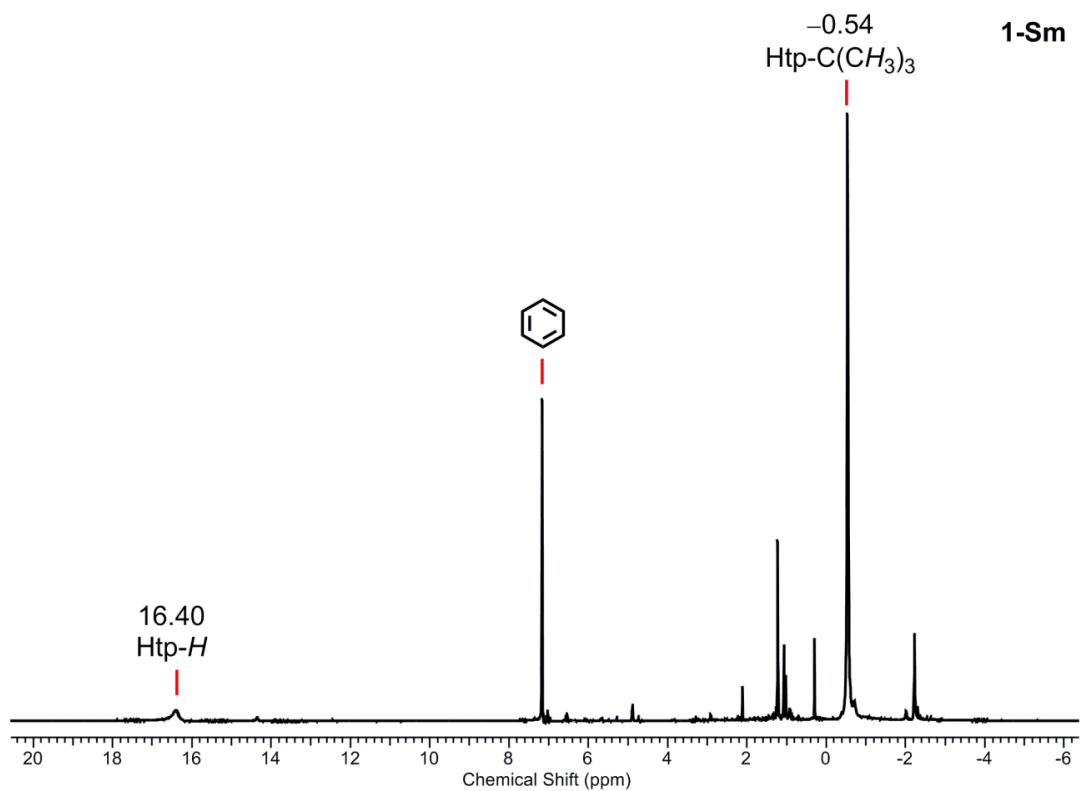


Figure S24. ¹H NMR spectrum of **1-Sm** in C₆D₆ in the region -6 to 20 ppm. Solvent residual marked.

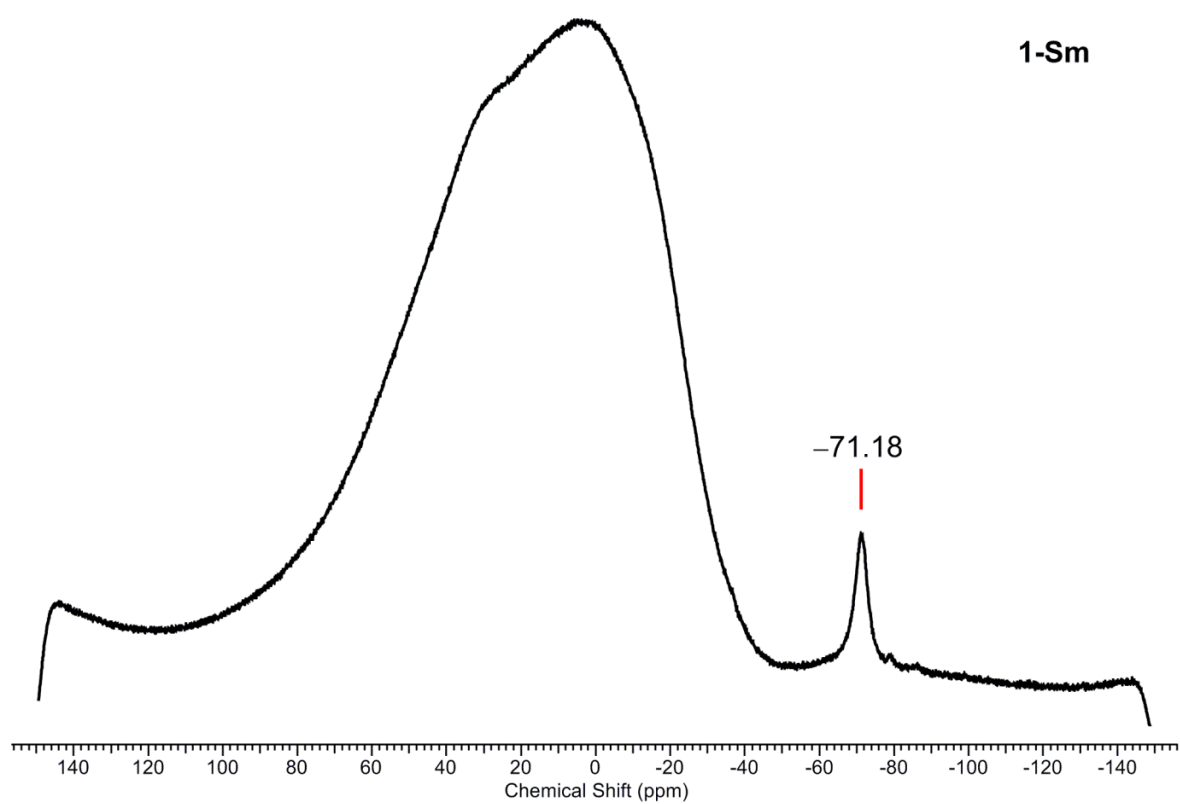


Figure S25. ¹¹B{¹H} NMR spectrum of **1-Sm** in C₆D₆.

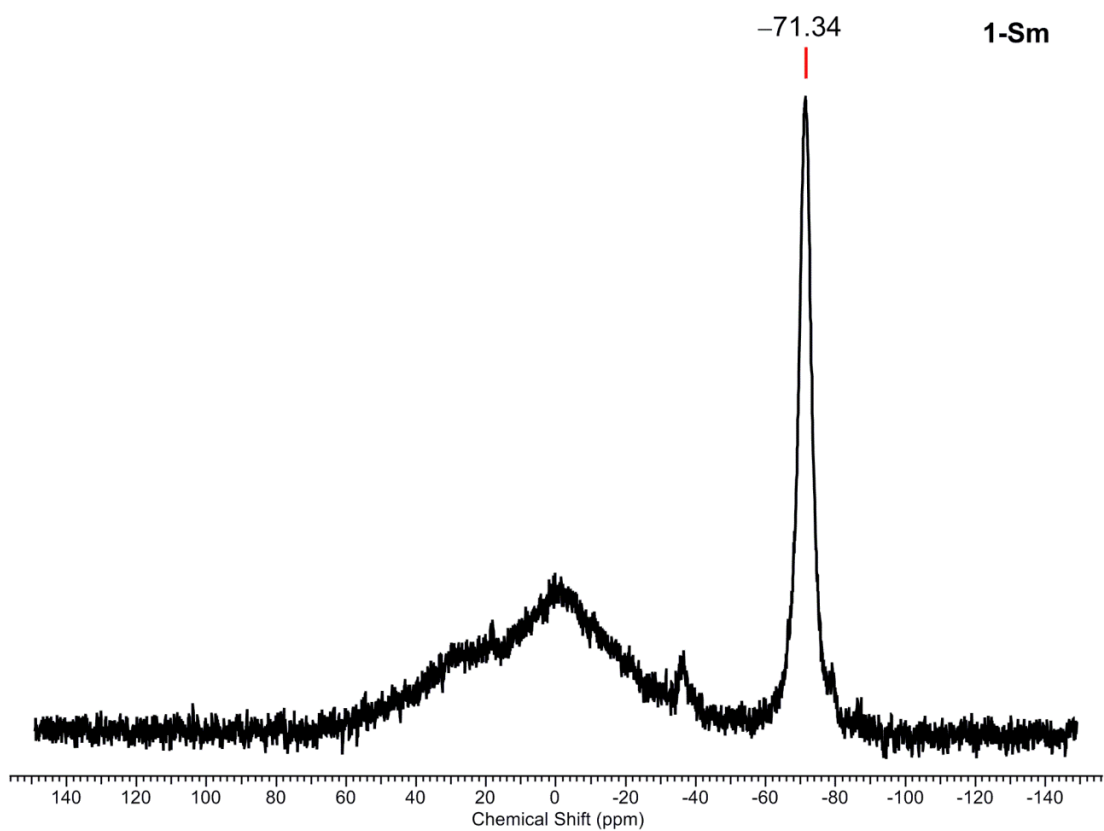


Figure S26. ¹¹B NMR spectrum of **1-Sm** in C₆D₆.

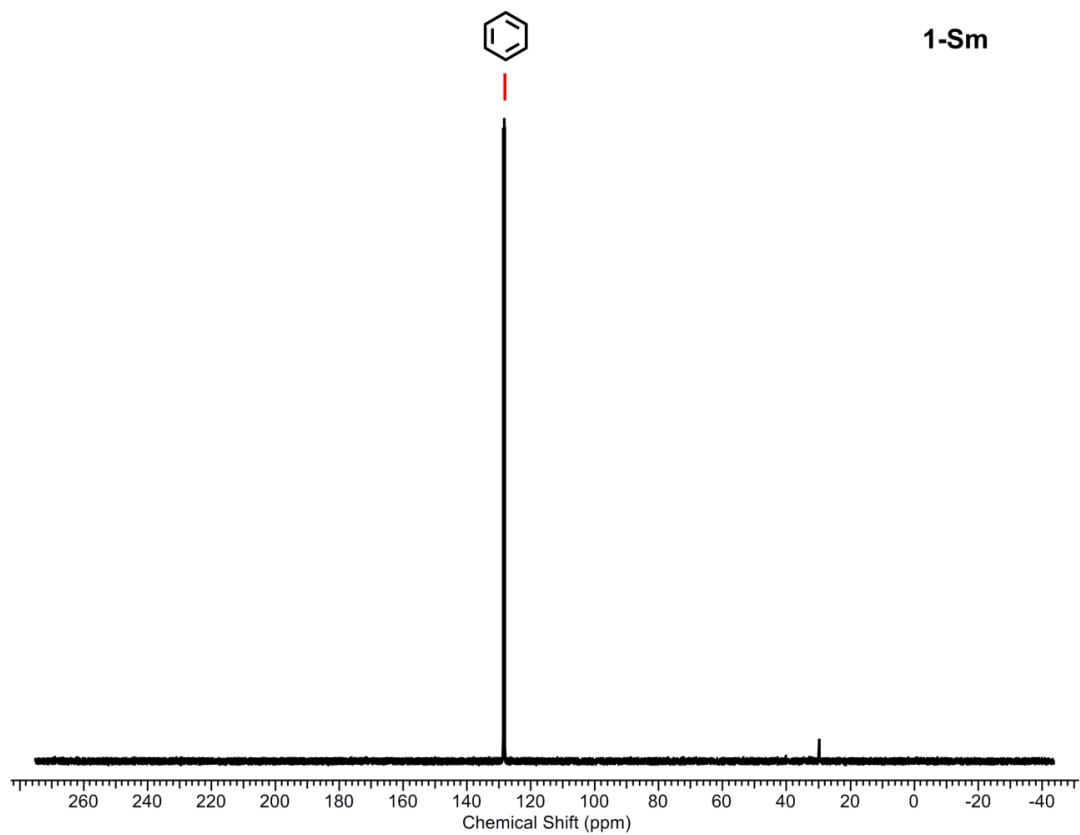


Figure S27. ¹³C{¹H} NMR spectrum of **1-Sm** in C₆D₆. Solvent residual marked.

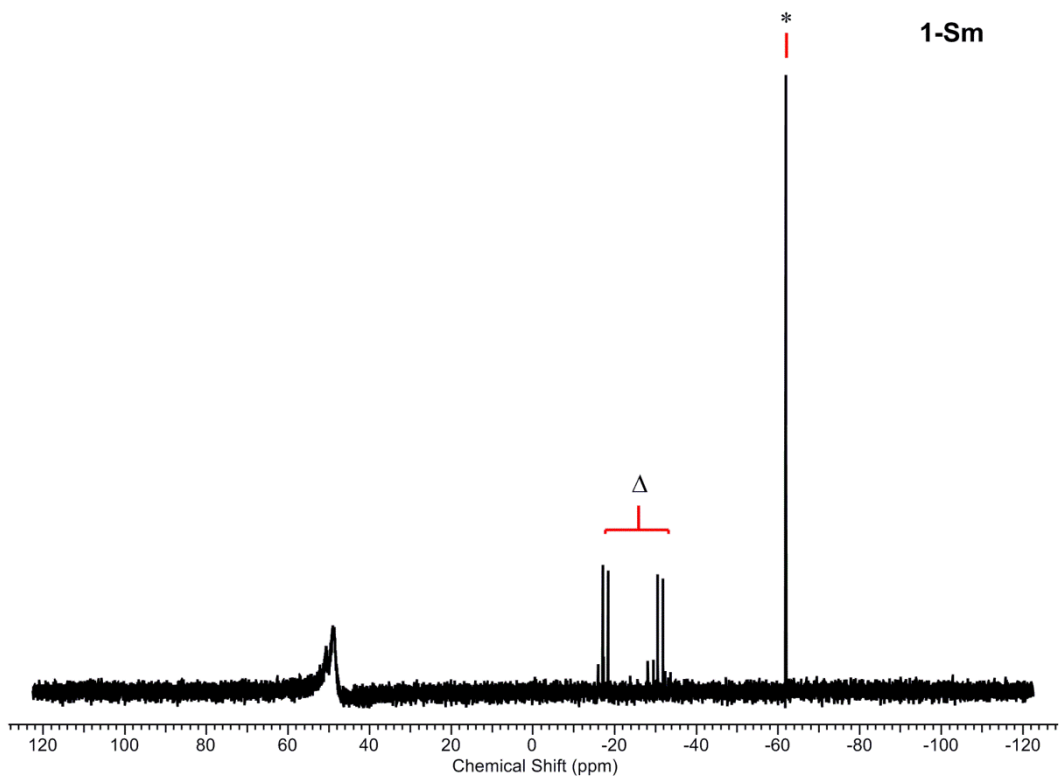


Figure S28. $^{31}\text{P}\{^1\text{H}\}$ NMR spectrum of **1-Sm** in C_6D_6 . * denotes diamagnetic impurities. Δ denotes $(\text{Htp})_2$ impurity.

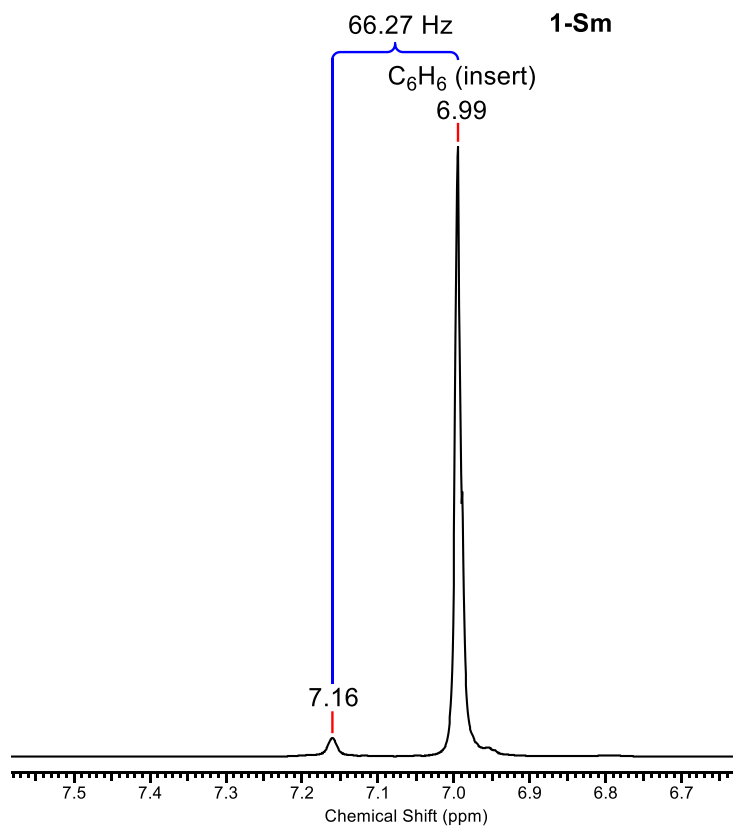


Figure S29. ^1H NMR spectrum of **1-Sm** in C_6D_6 with a $\text{C}_6\text{H}_6/\text{C}_6\text{D}_6$ insert. Solvent residual marked.

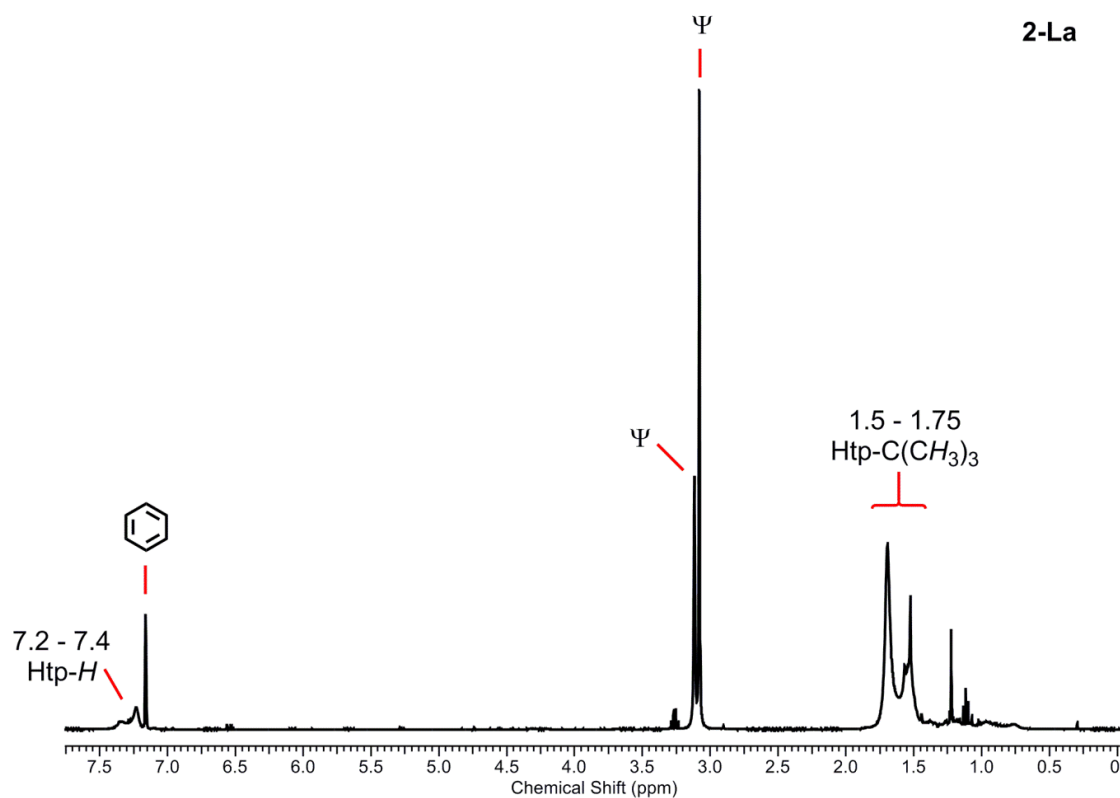


Figure S30. ^1H NMR spectrum of **2-La** in C_6D_6 in the region 0 to 7.5 ppm. Solvent residual marked. Ψ denotes DME of recrystallization.

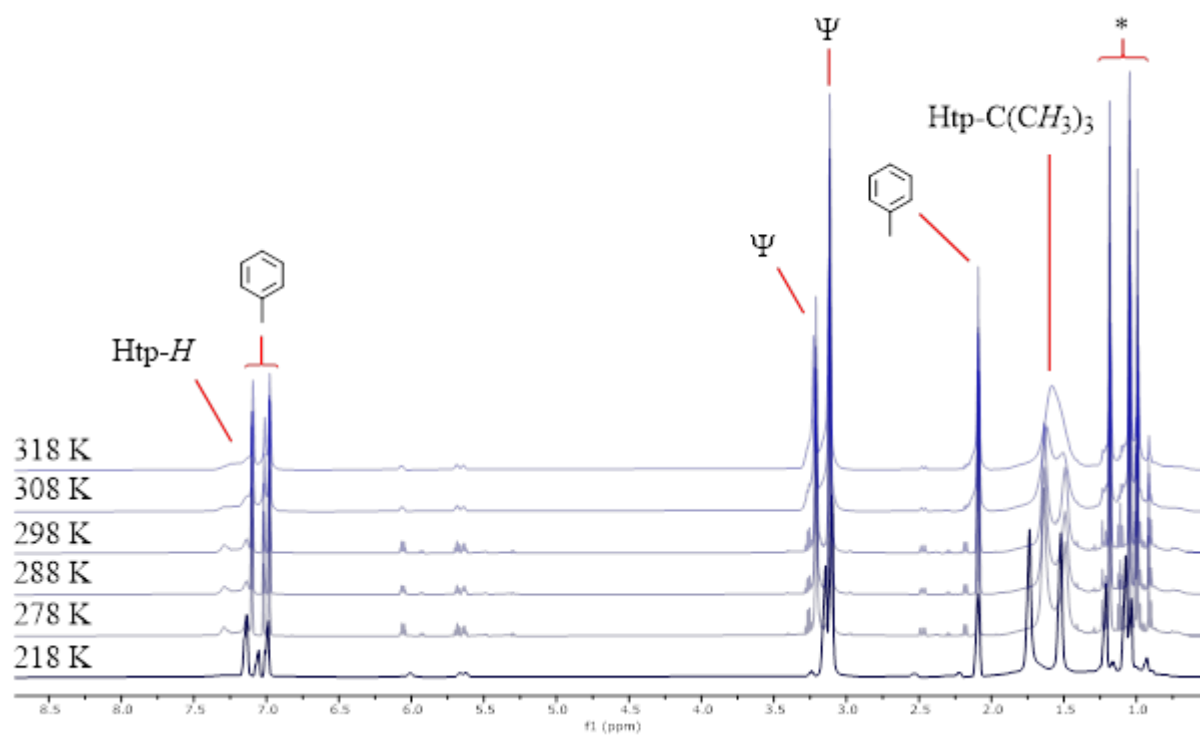


Figure S31. Variable temperature (218, 278 – 318 K) ^1H NMR spectra of **2-La** in C_7D_8 in the region 0 to 8.5 ppm. Ψ denotes DME of recrystallization, * denotes diamagnetic impurities.

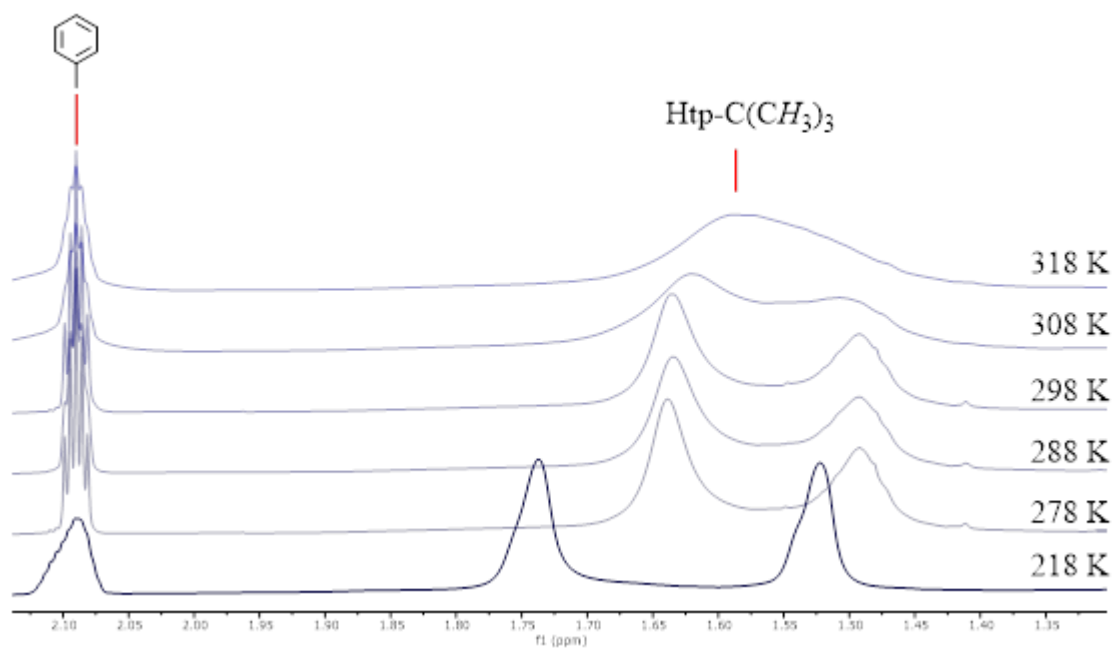


Figure S32. Variable temperature (218, 278 – 318 K) ^1H NMR spectra of **2-La** in C_7D_8 in the region 1.35 to 2.15 ppm.

The rate constant for rotation of the Htp ligands in **2-La** was calculated using an slow exchange regime, where $k = \pi(w_e - w_0)$ (Table S4; w_0 is the half height line width where no Htp rotation is occurring and w_e is the half height line width where rotation of the Htp ligands is occurring). Temperatures below 278 K showed no significant change in line width and so are not included in this calculation. The average line width of the two resonances was used as they are both part of one fluctuation. The half-height line width for each resonances was estimated using MestReNova.⁷ The plot of $\ln(k/T)$ vs. $1/T$ (Figure S33) yielded the rotational enthalpy barrier of 31(7) kJ mol^{-1} and activation energy of 33(7) kJ mol^{-1} (generated from plot of $\ln(k)$ vs. $1/T$).⁸

Table S4. Rate constants determined from variable temperature NMR data of **2-La** in C_7D_8 .

Temp / K	218	278	288	298	308	318
w / Hz	12.53 (w_0)	18.13	21.50	20.56	37.15	45.68
k / s^{-1}	0	17.58	28.16	25.23	77.33	104.96

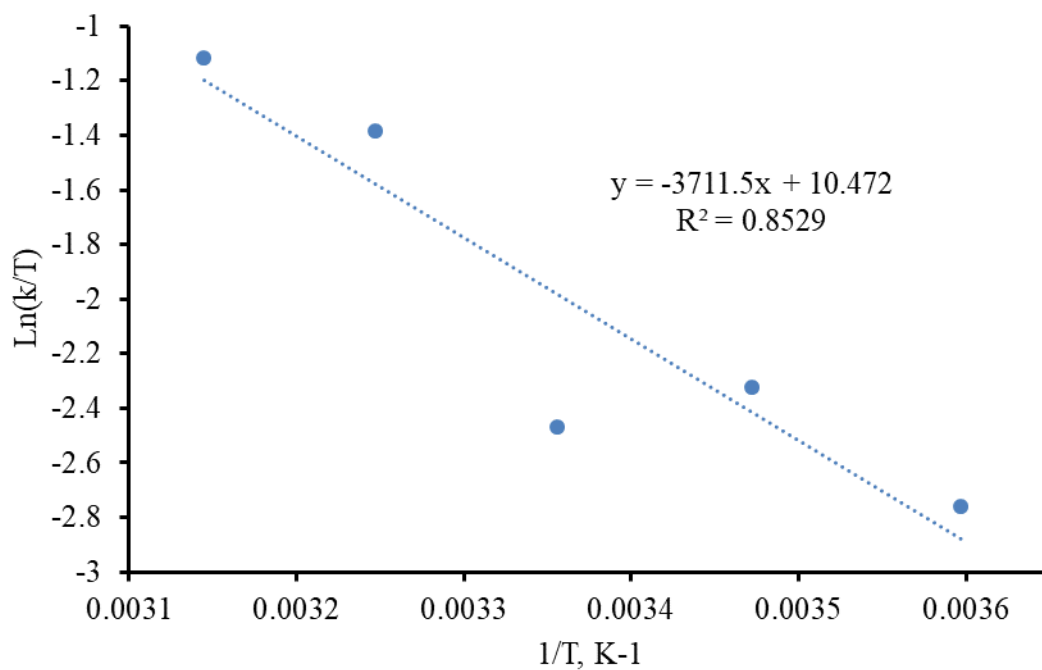


Figure S33. $\log(k/T)$ vs. $1/T$ (K^{-1}) calculated from variable temperature NMR data of **2-La** in C_7D_8 .

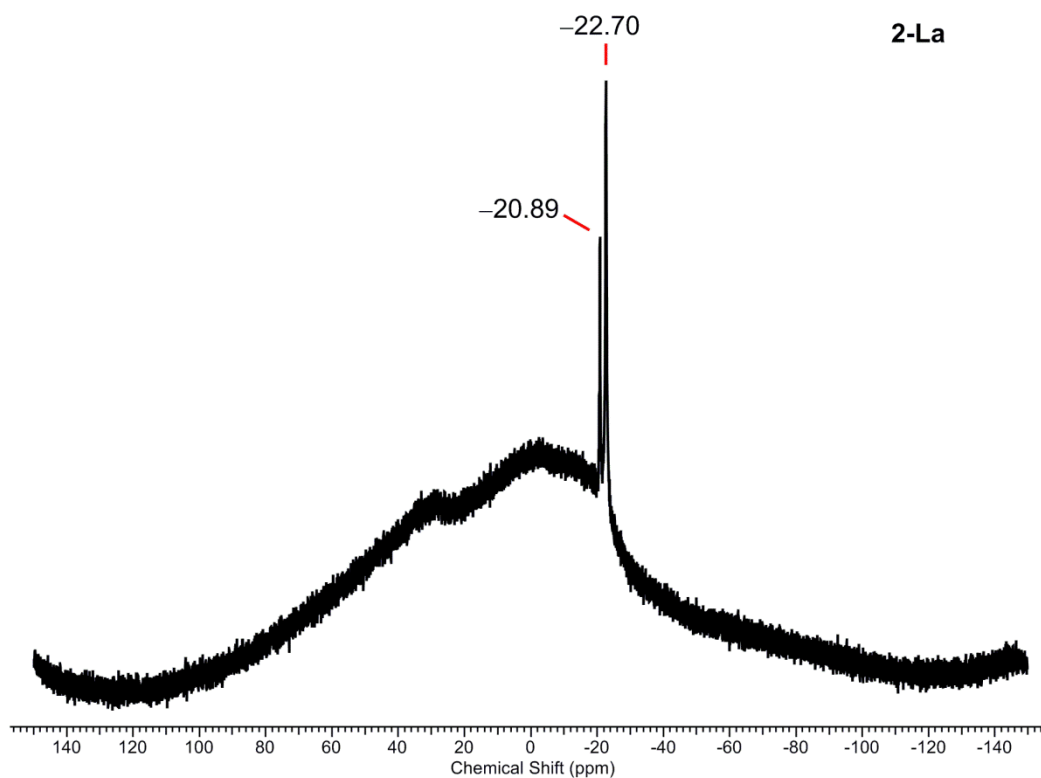


Figure S34. $^{11}B\{^1H\}$ NMR spectrum of **2-La** in C_6D_6 .

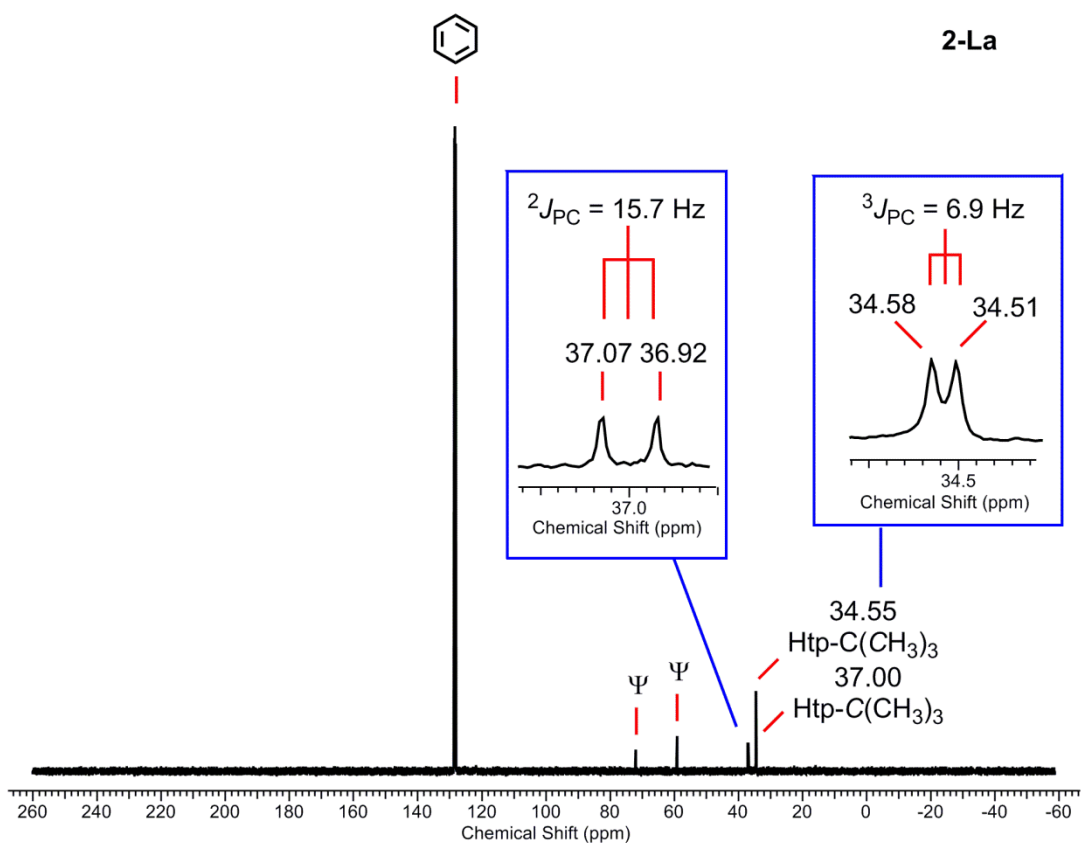


Figure S35. $^{13}\text{C}\{^1\text{H}\}$ NMR spectrum of **2-La** in C_6D_6 . Solvent residual marked. Ψ denotes DME of recrystallization.

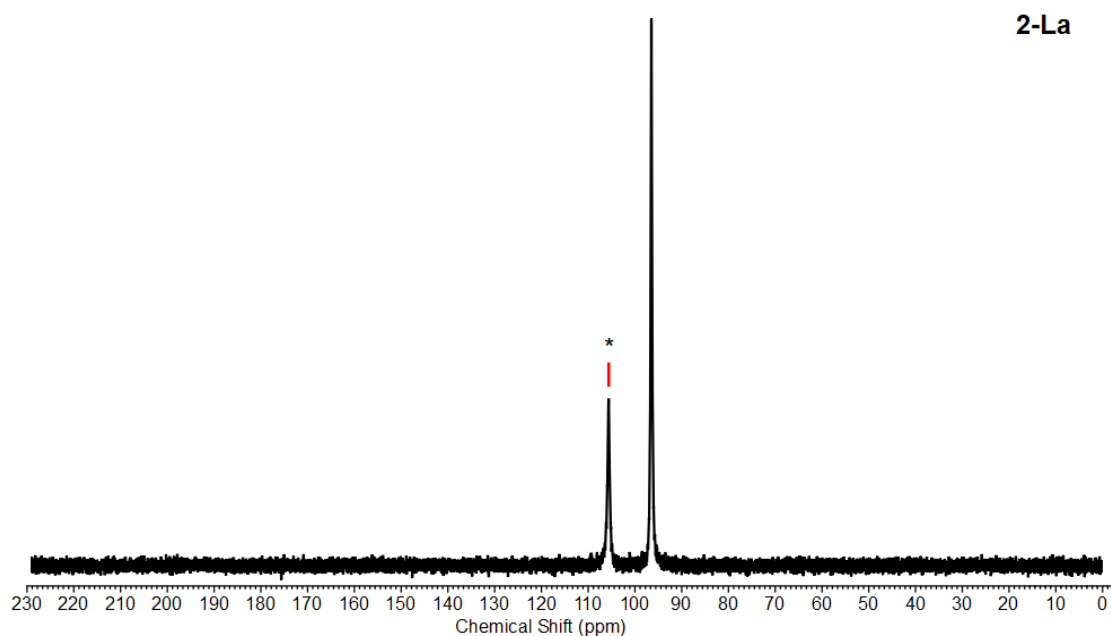


Figure S36. $^{31}\text{P}\{^1\text{H}\}$ NMR spectrum of **2-La** in C_6D_6 . * denotes **1-La** impurity.

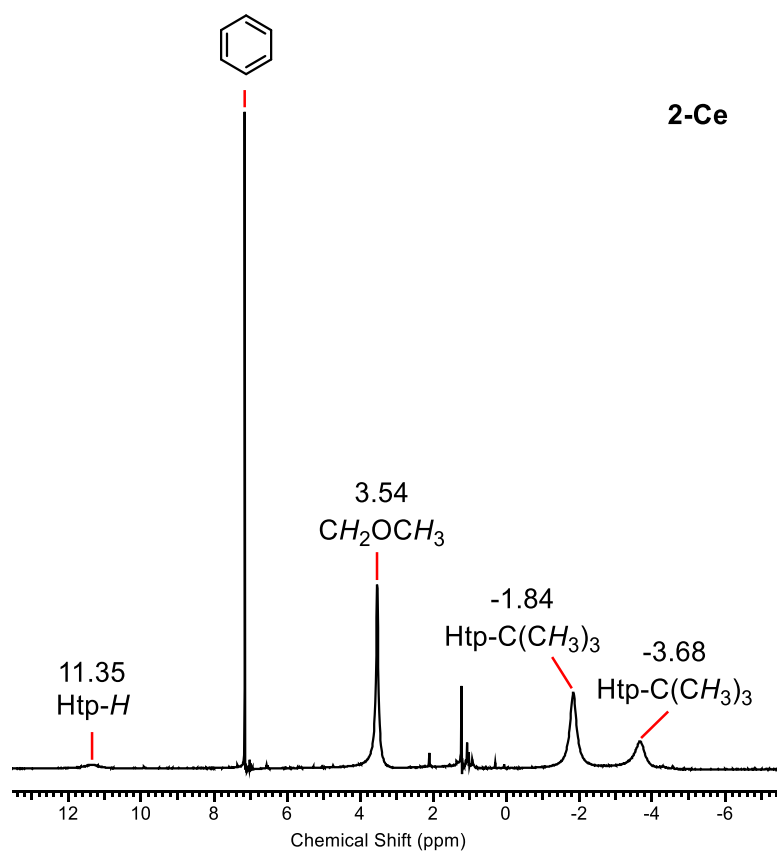


Figure S37. 1H NMR spectrum of **2-Ce** in C_6D_6 in the region -6 to 12 ppm. Solvent residual marked.

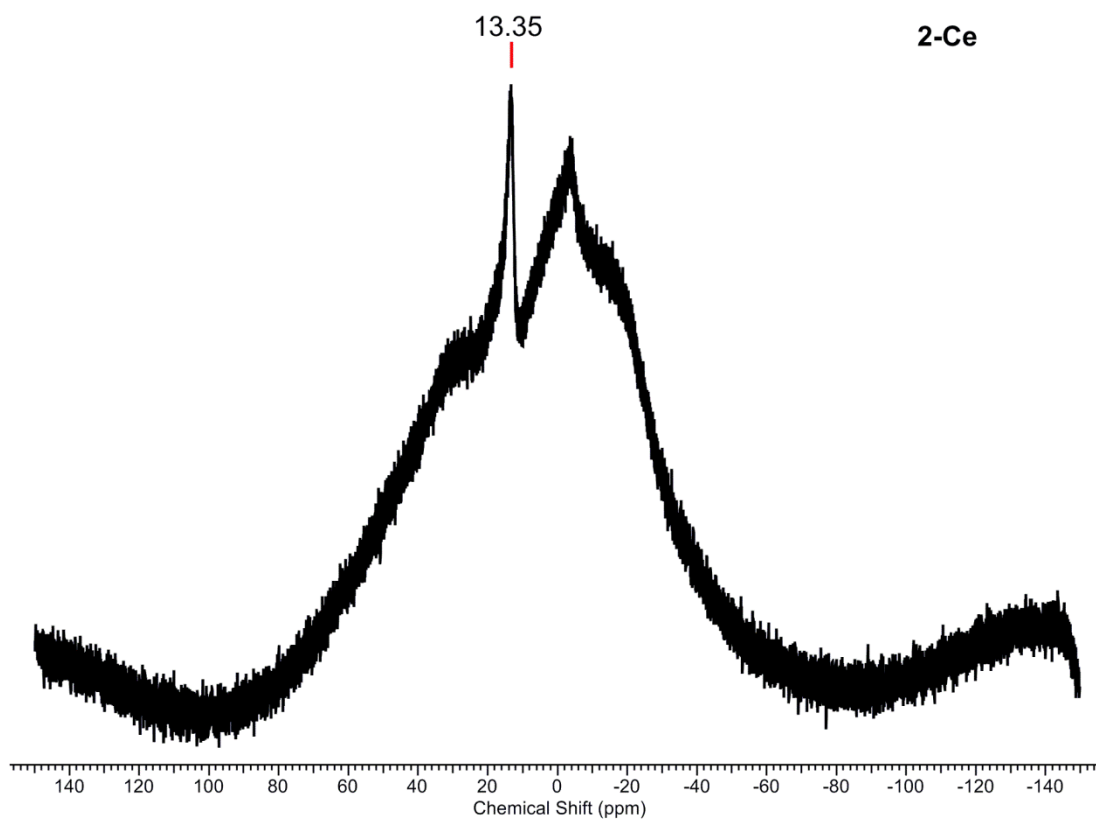


Figure S38. $^{11}B\{^1H\}$ NMR spectrum of **2-Ce** in C_6D_6 .

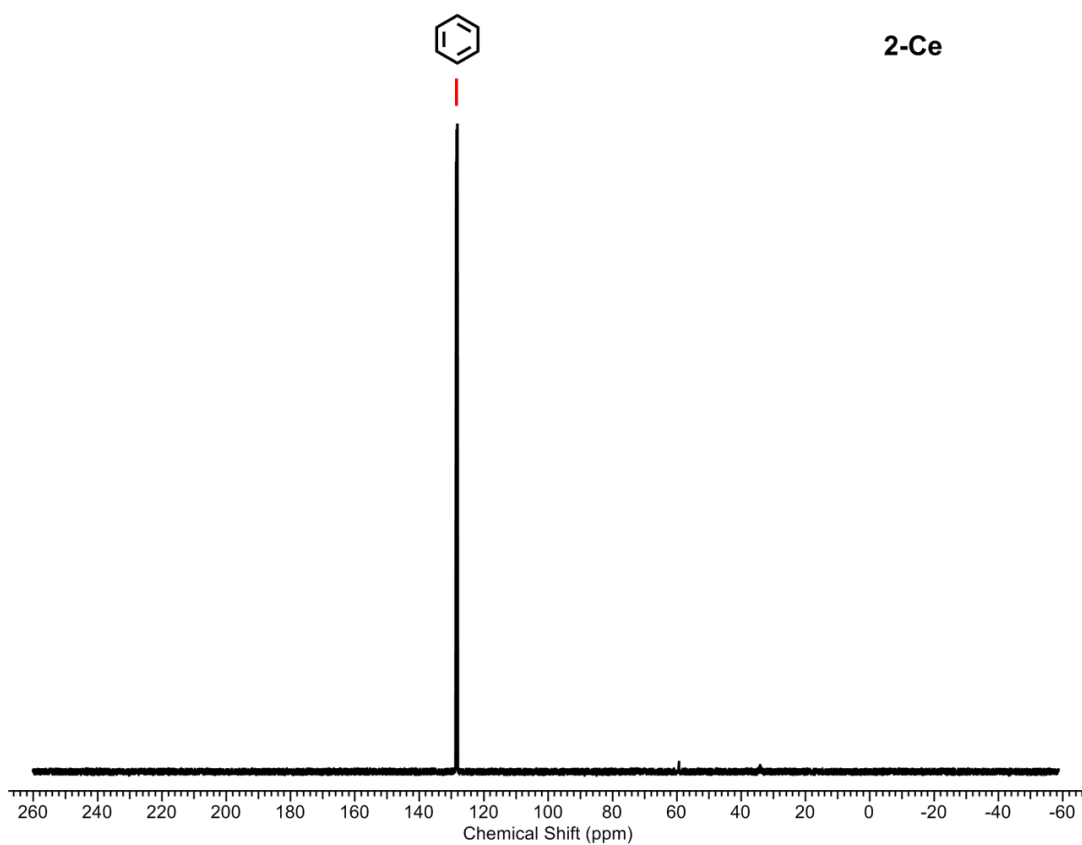


Figure S39. $^{13}\text{C}\{^1\text{H}\}$ NMR spectrum of **2-Ce** in C_6D_6 . Solvent residual marked.

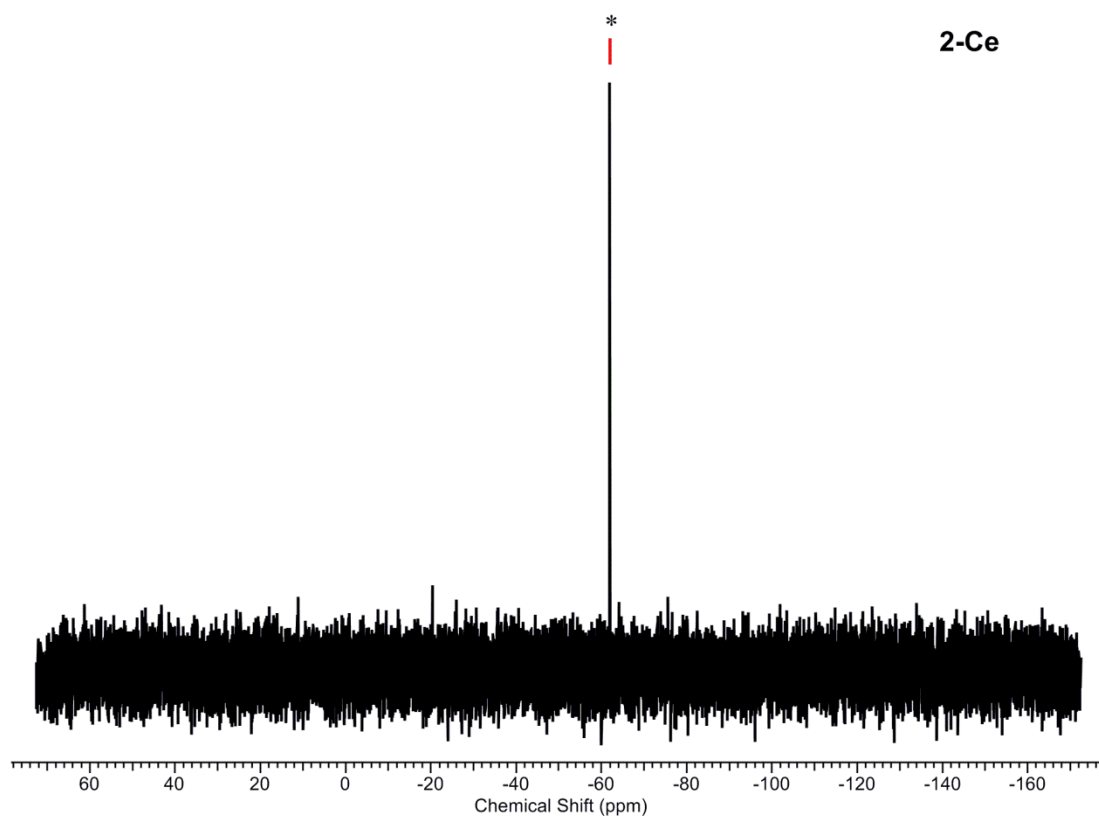


Figure S40. $^{31}\text{P}\{^1\text{H}\}$ NMR spectrum of **2-Ce** in C_6D_6 . * denotes diamagnetic impurities.

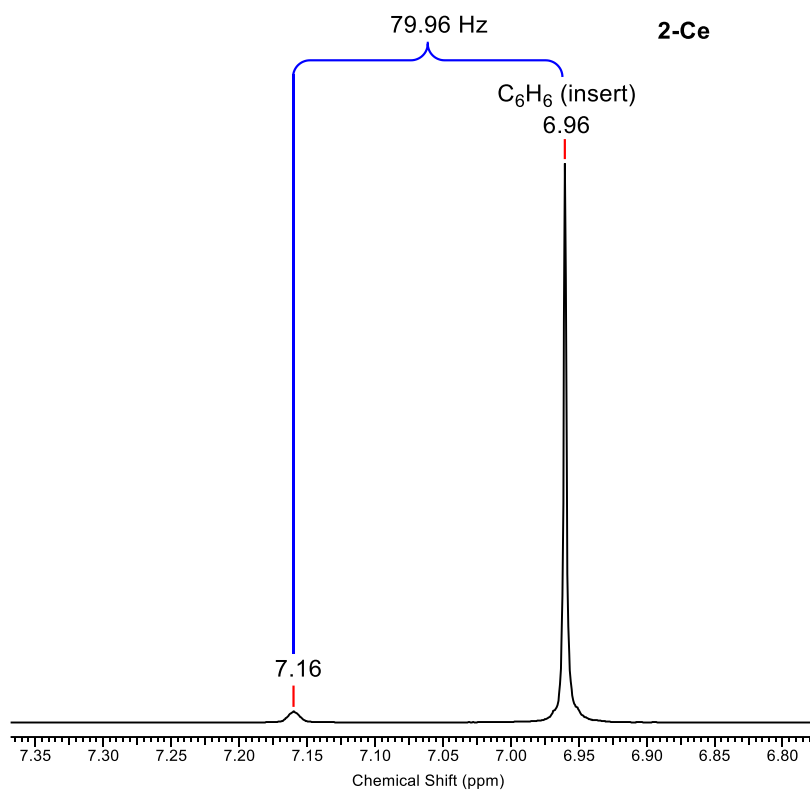


Figure S41. ¹H NMR spectrum of **2-Ce** in C₆D₆ with a C₆H₆/C₆D₆ insert. Solvent residual marked.

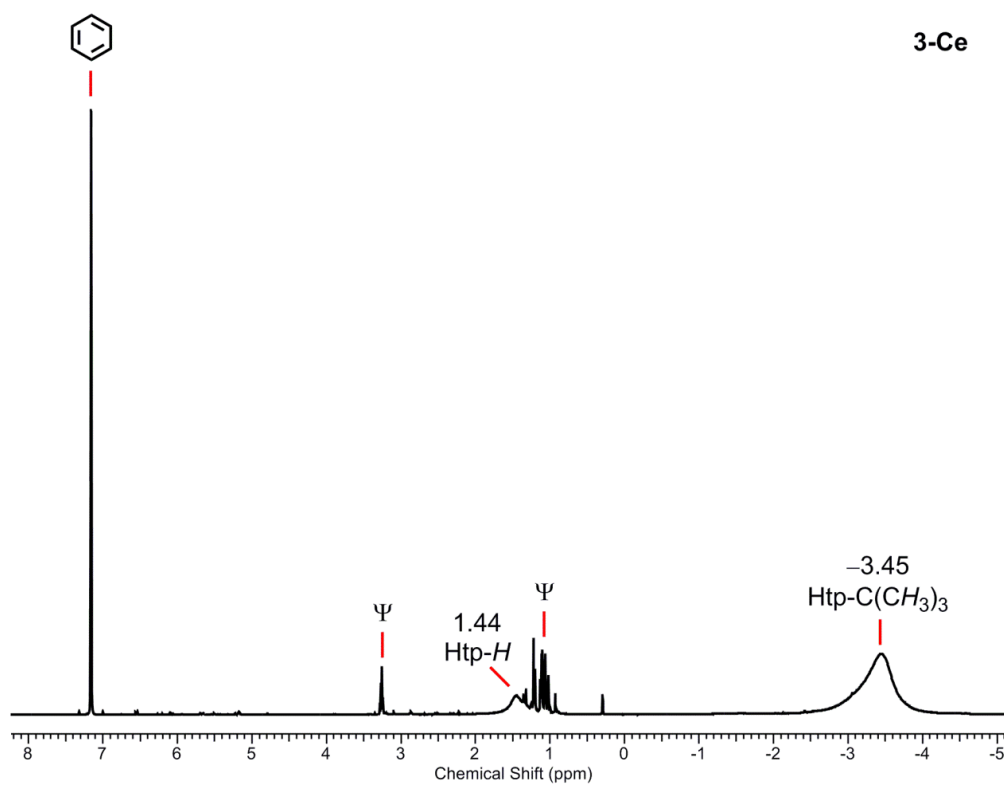


Figure S42. ¹H NMR spectrum of **3-Ce** in C₆D₆ zoomed in the region -5 to 8 ppm. Solvent residual marked. Ψ denotes Et₂O of recrystallization.

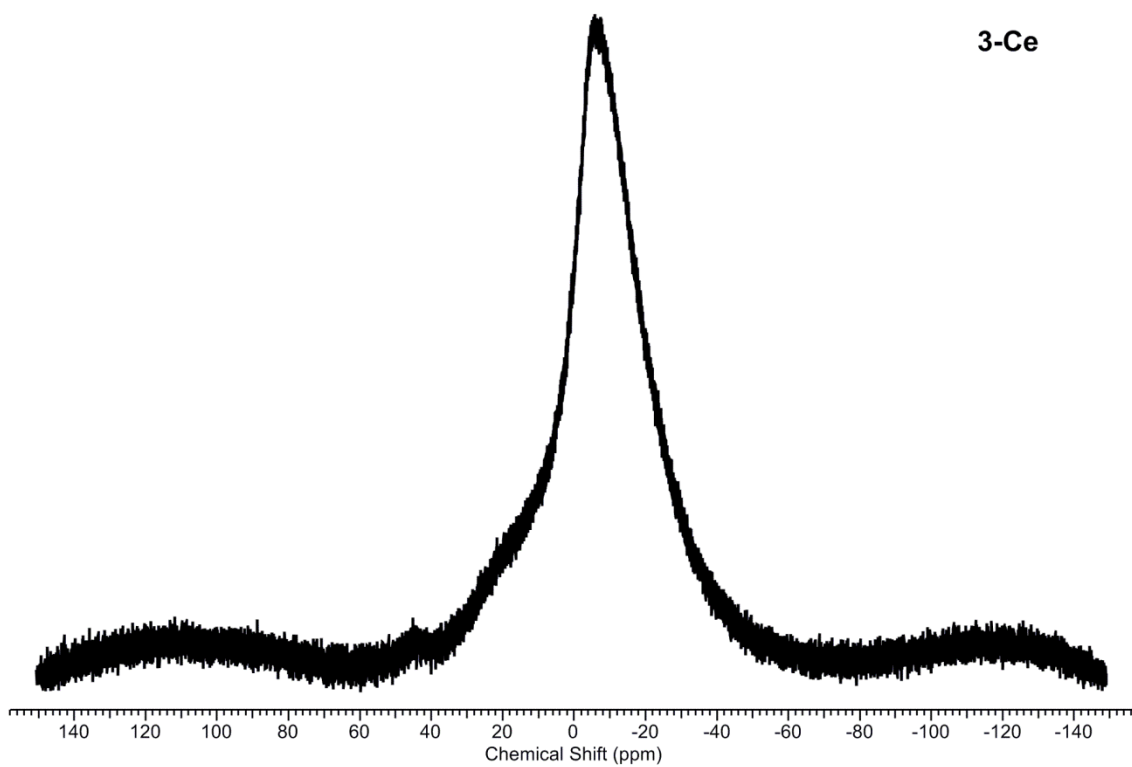


Figure S43. $^{11}\text{B}\{^1\text{H}\}$ NMR spectrum of **3-Ce** in C_6D_6 .

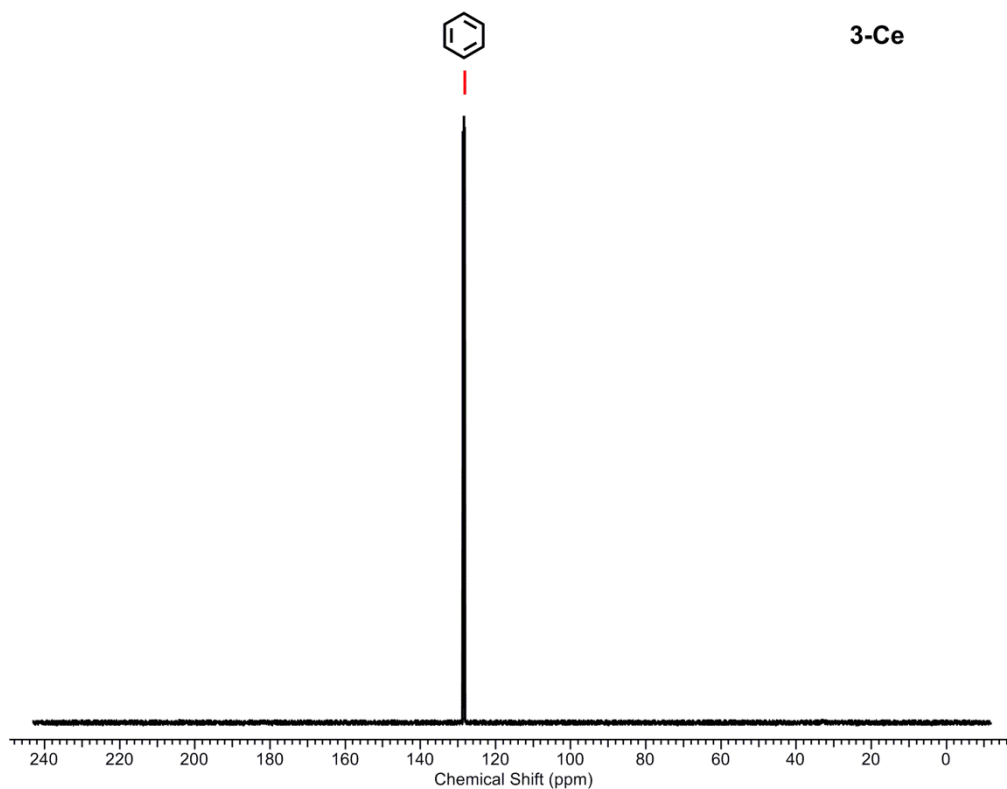


Figure S44. $^{13}\text{C}\{^1\text{H}\}$ NMR spectrum of **3-Ce** in C_6D_6 . Solvent residual marked.

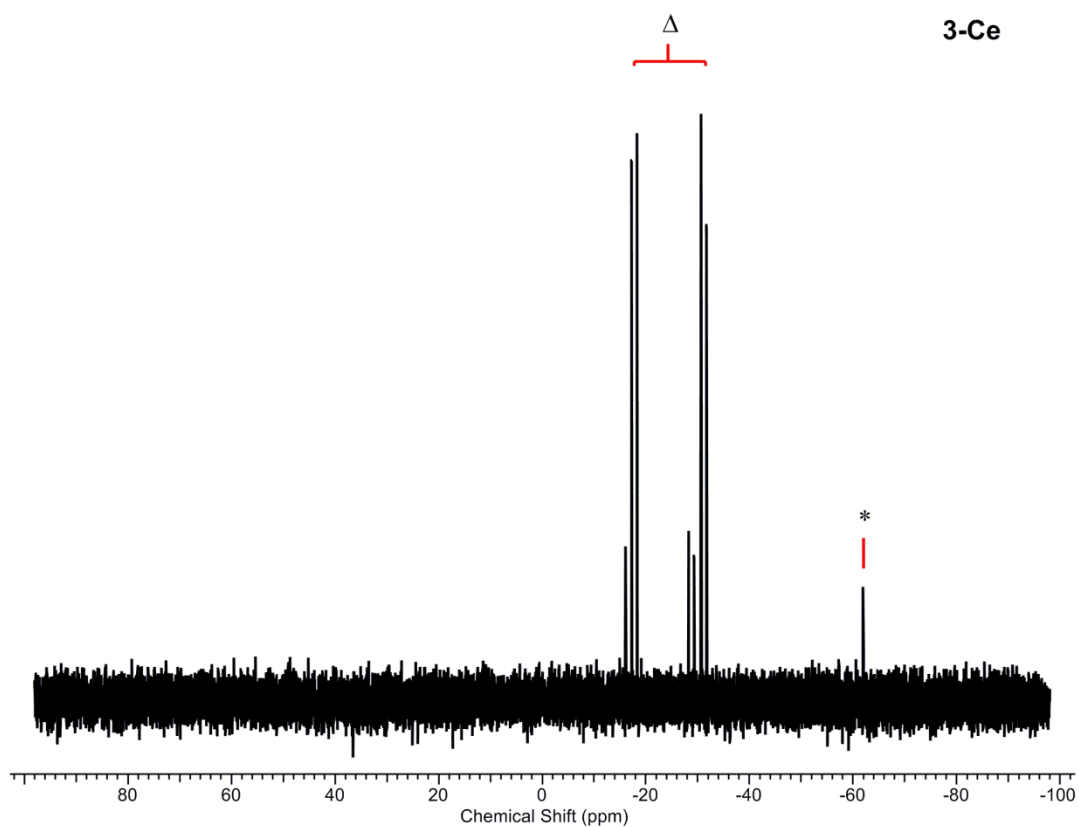


Figure S45. $^{31}\text{P}\{^1\text{H}\}$ NMR spectrum of **3-Ce** in C_6D_6 . * denotes diamagnetic impurities. Δ denotes $(\text{Htp})_2$ impurity.

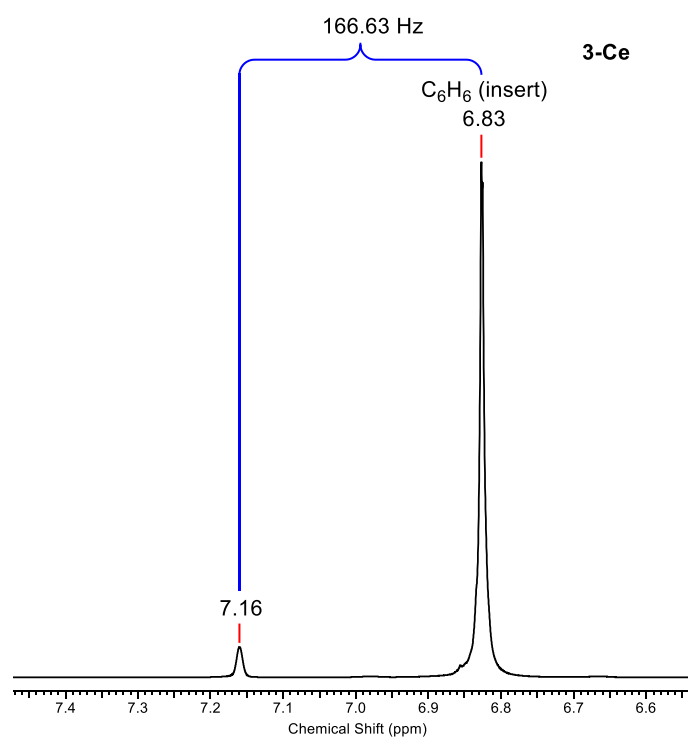


Figure S46. ^1H NMR spectrum of **3-Ce** in C_6D_6 with a $\text{C}_6\text{H}_6/\text{C}_6\text{D}_6$ insert. Solvent residual marked.

6. ATR-IR spectroscopy

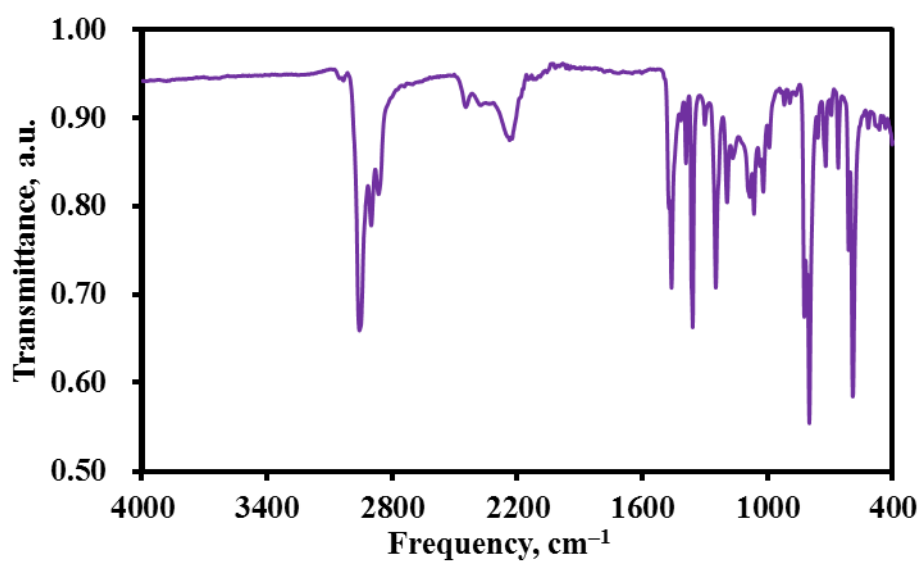


Figure S47. ATR-IR spectrum of **1-La** recorded as a microcrystalline powder.

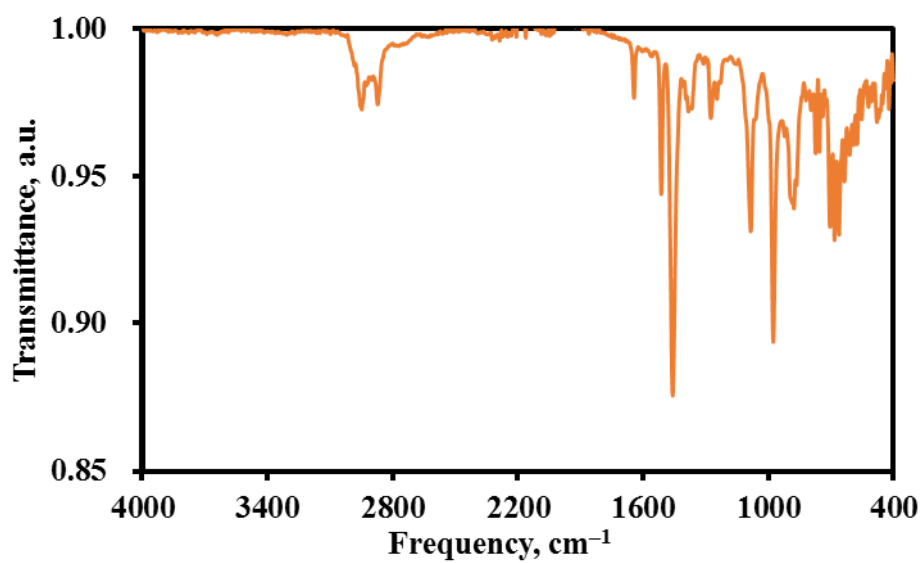


Figure S48. ATR-IR spectrum of **1-Ce** recorded as a microcrystalline powder.

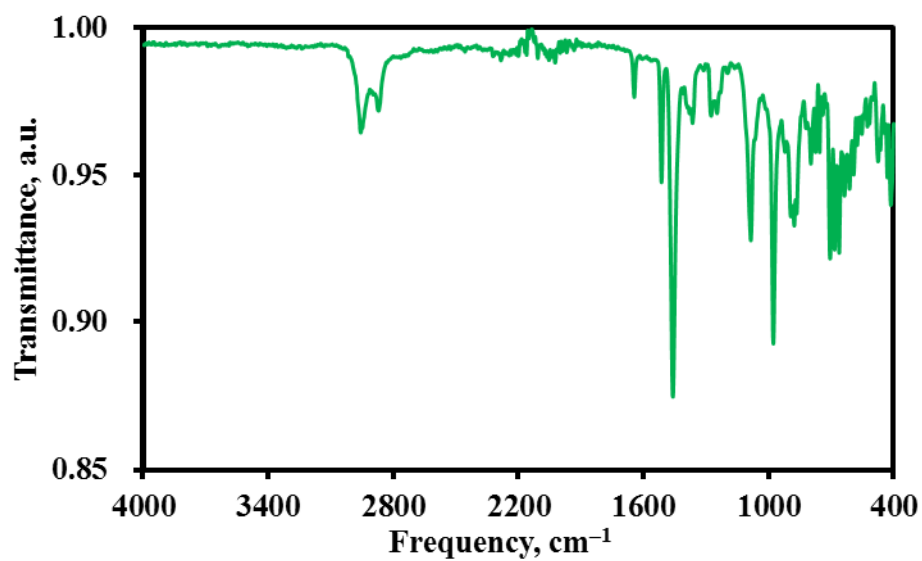


Figure S49. ATR-IR spectrum of **1-Nd** recorded as a microcrystalline powder.

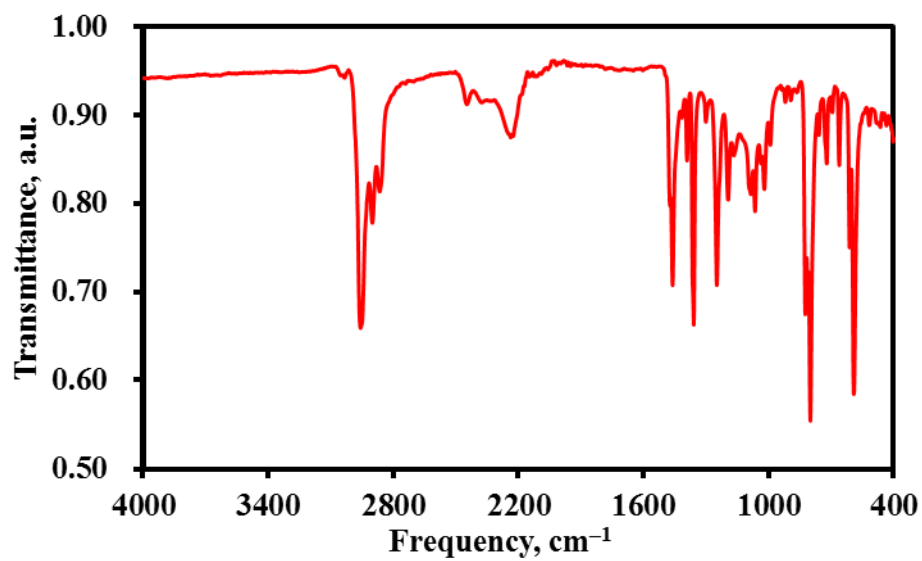


Figure S50. ATR-IR spectrum of **1-Sm** recorded as a microcrystalline powder.

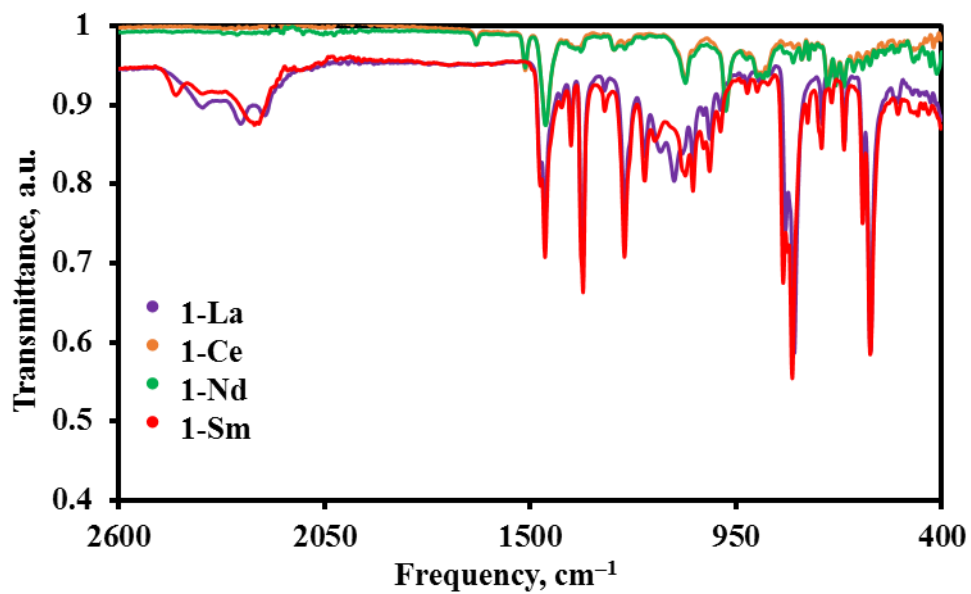


Figure S51. ATR-IR spectra of **1-La**, **1-Ce**, **1-Nd**, **1-Sm** in the region 2600–400 cm^{-1} intended to show the similarities between all spectra.

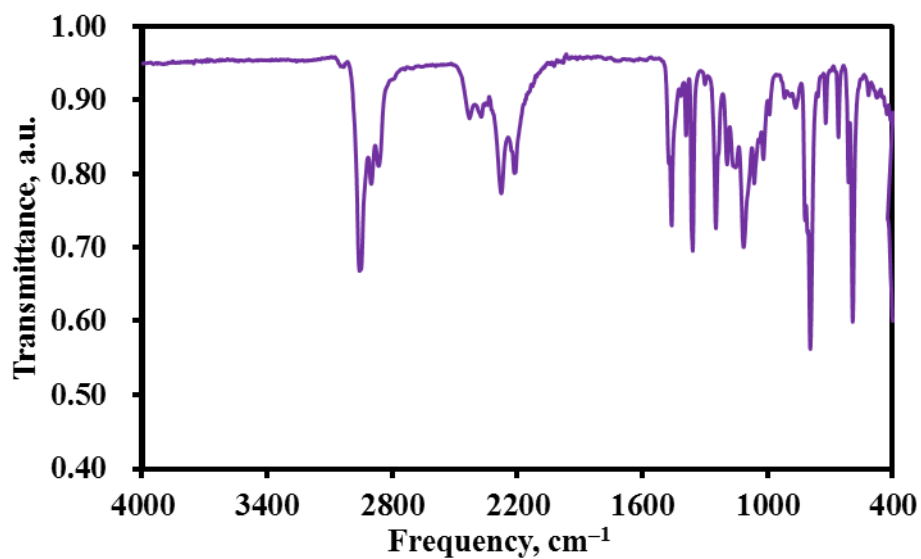


Figure S52. ATR-IR spectrum of **2-La** recorded as a microcrystalline powder.

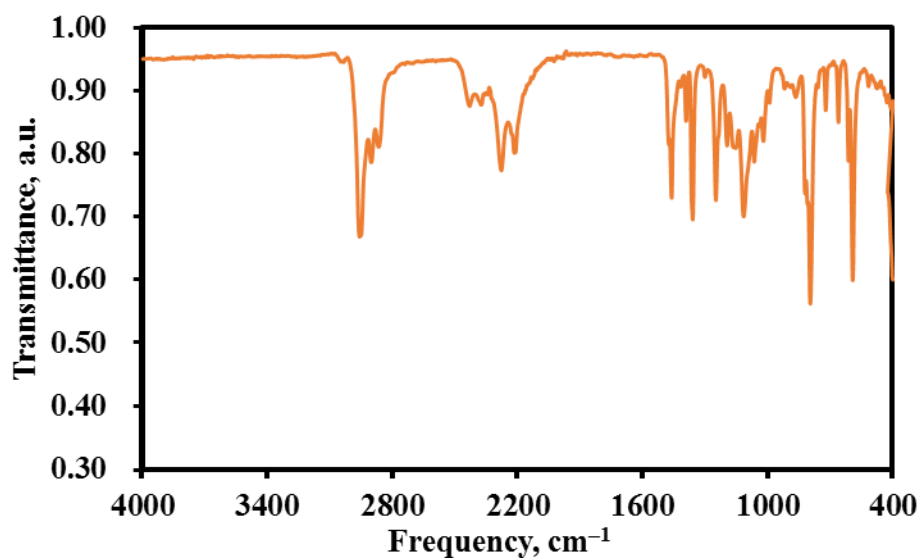


Figure S53. ATR-IR spectrum of 2-Ce recorded as a microcrystalline powder.

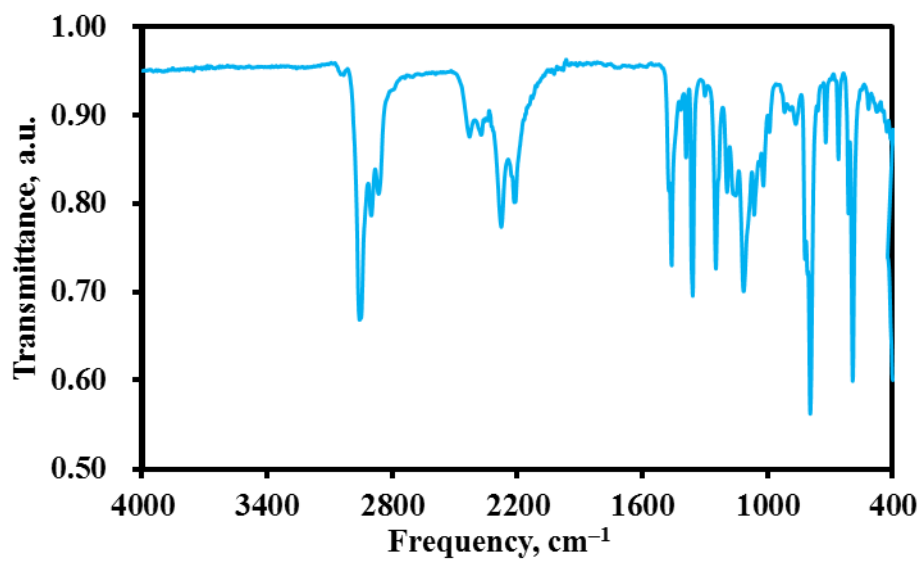


Figure S54. ATR-IR spectrum of 3-Ce recorded as a microcrystalline powder.

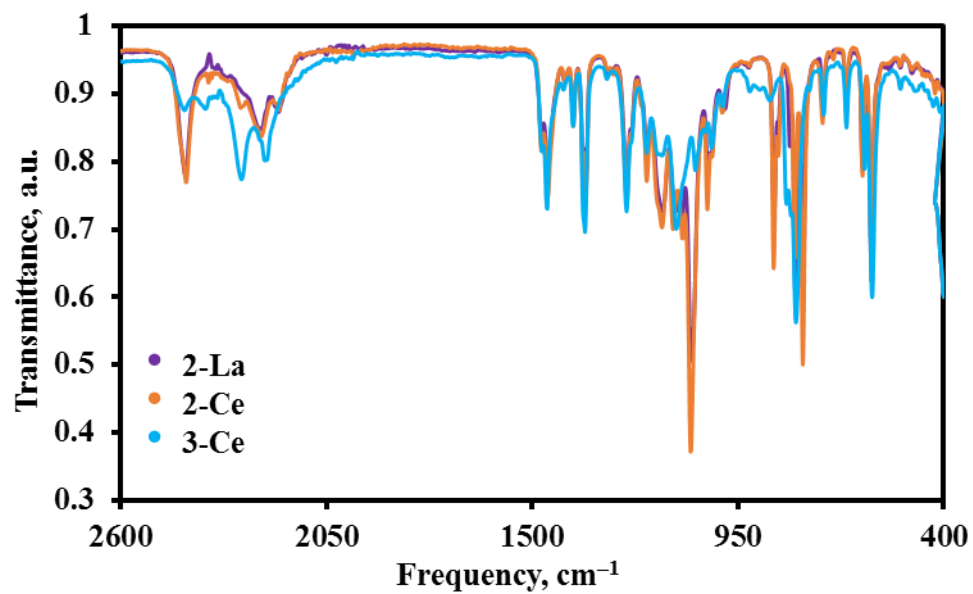


Figure S55. ATR-IR spectra of **2-La**, **2-Ce**, **3-Ce** in the region 2600–400 cm⁻¹ intended to show the similarities between all spectra.

7. UV-vis-NIR spectroscopy

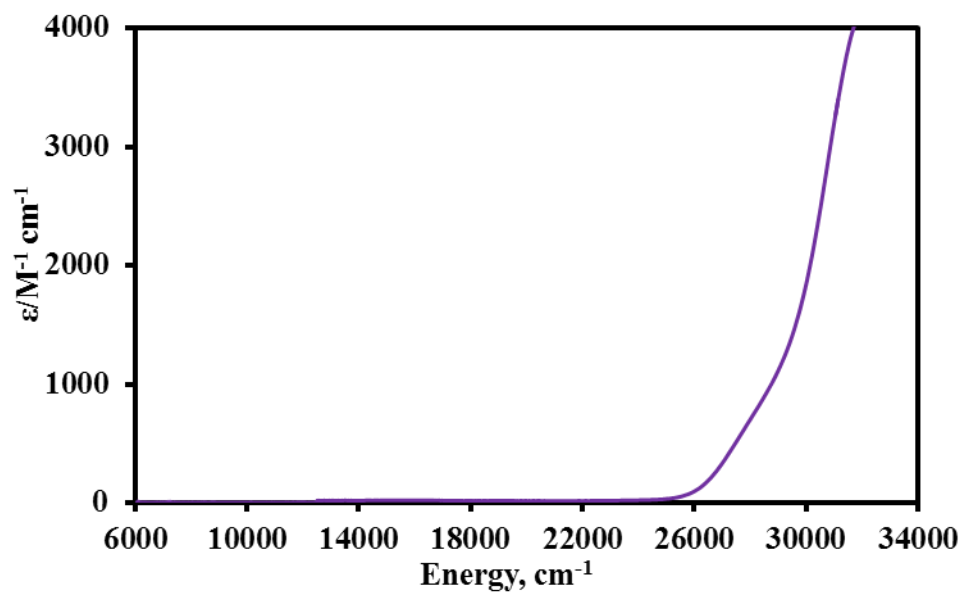


Figure S56. UV-vis-NIR spectrum of **1-La** between 34000–6000 cm^{-1} (295–1650 nm) recorded as a 0.5 mM solution in toluene.

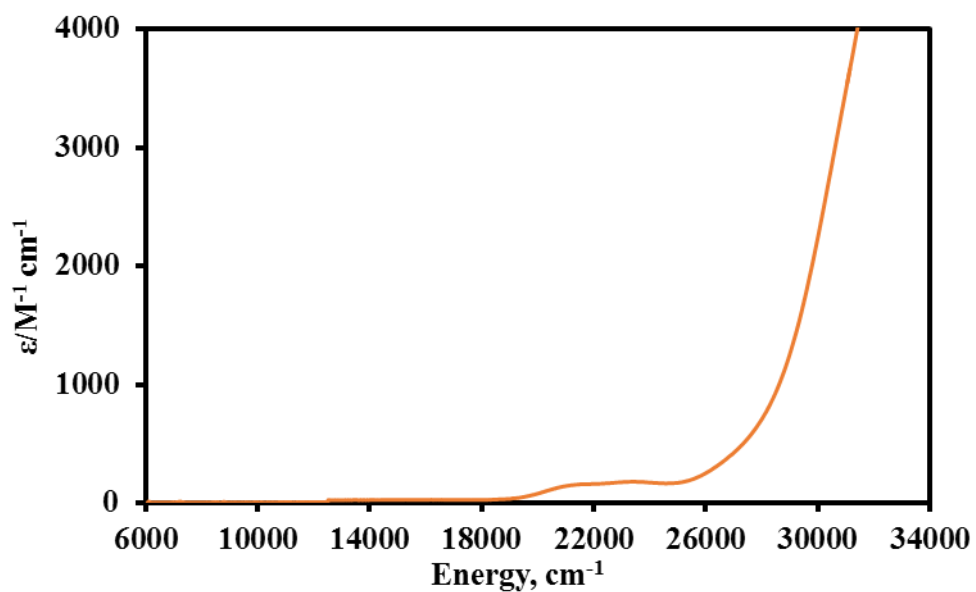


Figure S57. UV-vis-NIR spectrum of **1-Ce** between 34000–6000 cm^{-1} (295–1650 nm) recorded as a 0.5 mM solution in toluene.

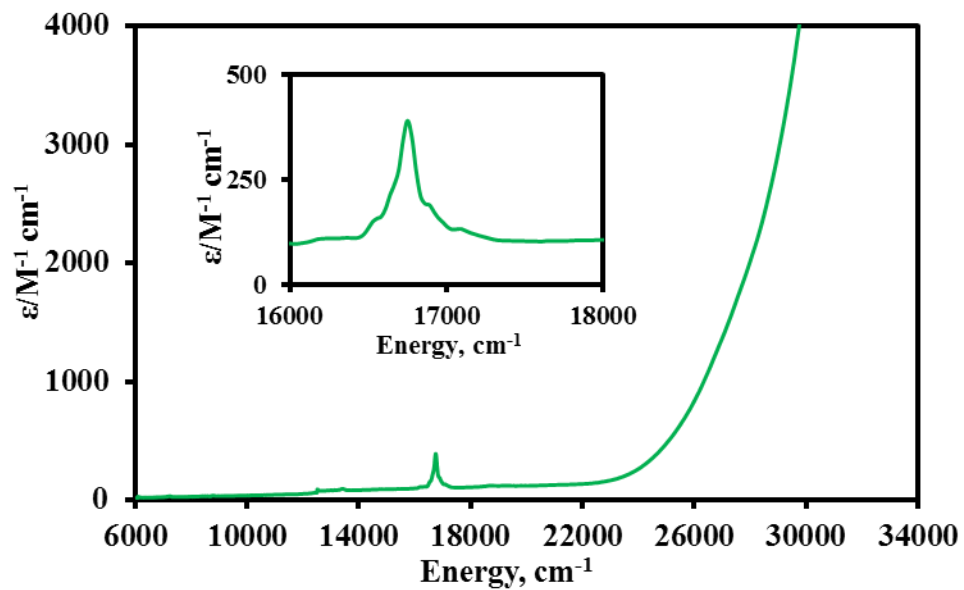


Figure S58. UV-vis-NIR spectrum of **1-Nd** between 34000–6000 cm^{-1} (295–1650 nm) recorded as a 0.5 mM solution in toluene.

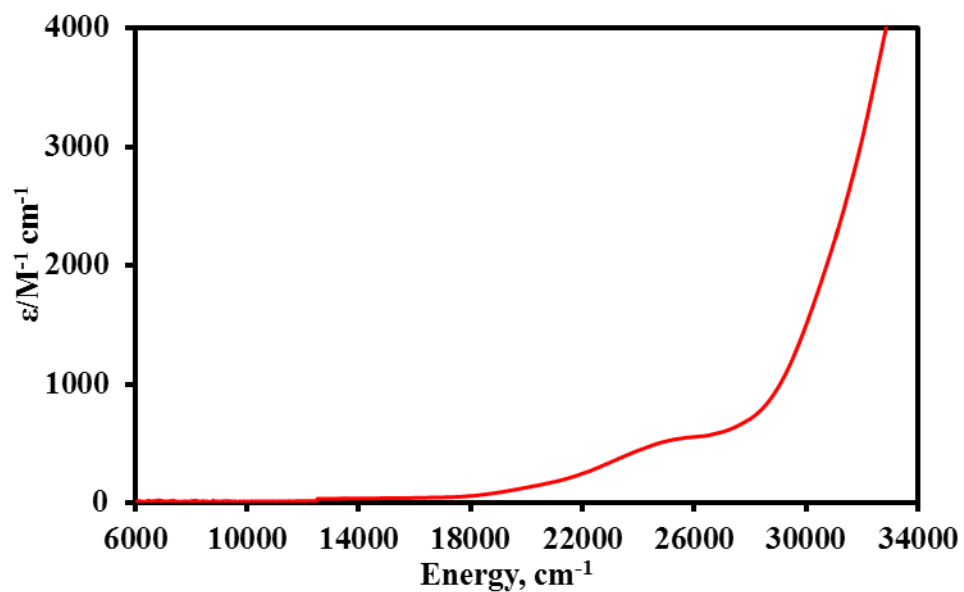


Figure S59. UV-vis-NIR spectrum of **1-Sm** between 34000–6000 cm^{-1} (295–1650 nm) recorded as a 0.5 mM solution in toluene.

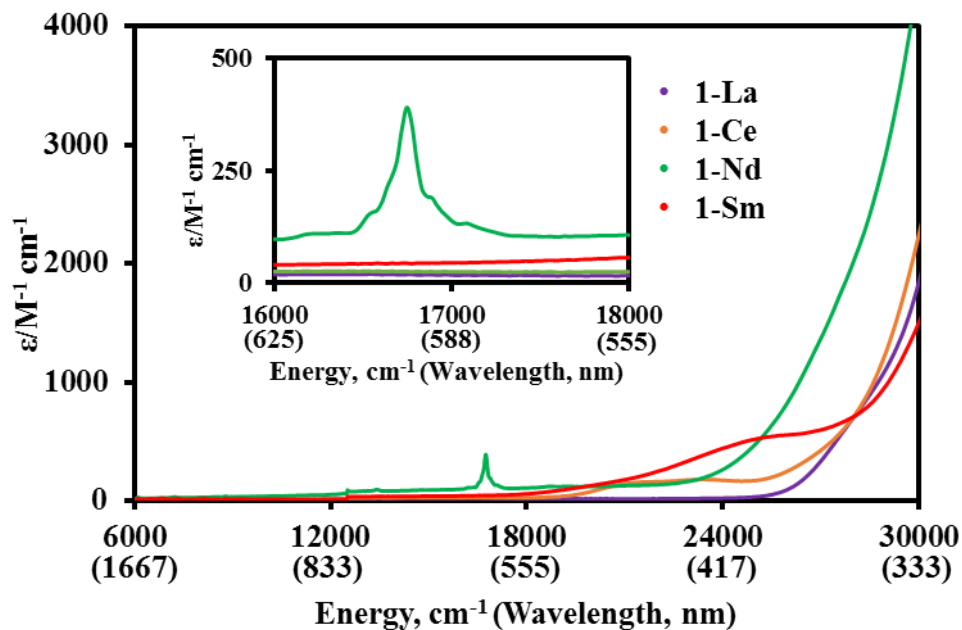


Figure S60. UV-vis-NIR spectrum of **1-La**, **1-Ce**, **1-Nd**, **1-Sm**, in the region 6000–30000 cm^{-1} (inset 16000–18000 showing main region) recorded in toluene at room temperature, concentrations listed above individually.

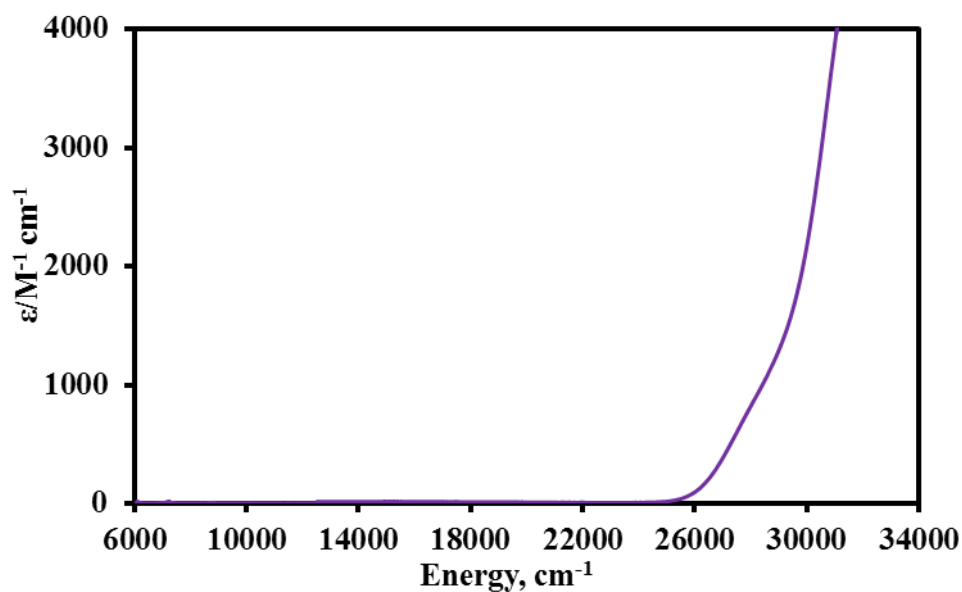


Figure S61. UV-vis-NIR spectrum of **2-La** between 34000–6000 cm^{-1} (295–1650 nm) recorded as a 0.5 mM solution in toluene.

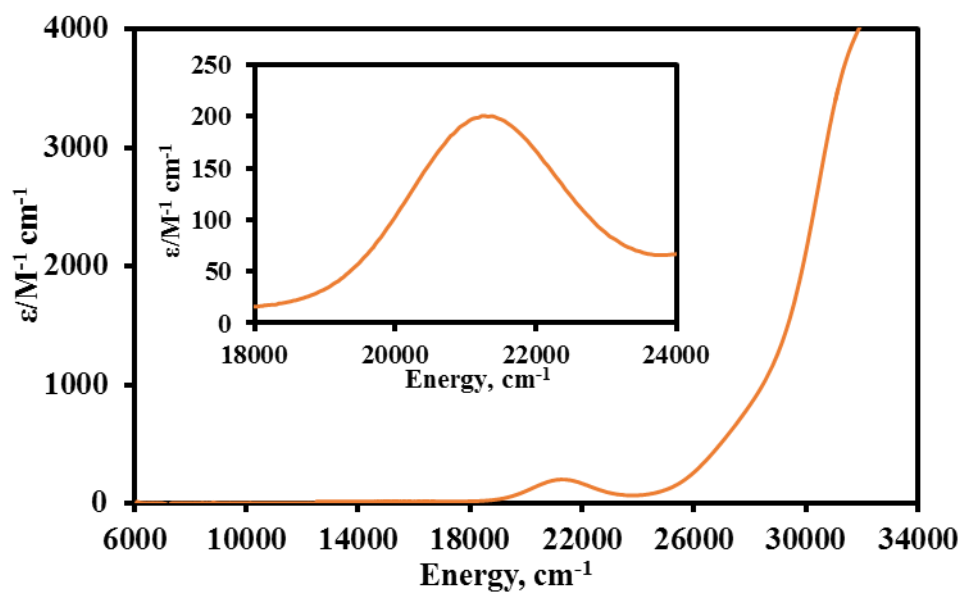


Figure S62. UV-vis-NIR spectrum of **2-Ce** between 34000–6000 cm^{-1} (295–1650 nm) recorded as a 0.5 mM solution in toluene.

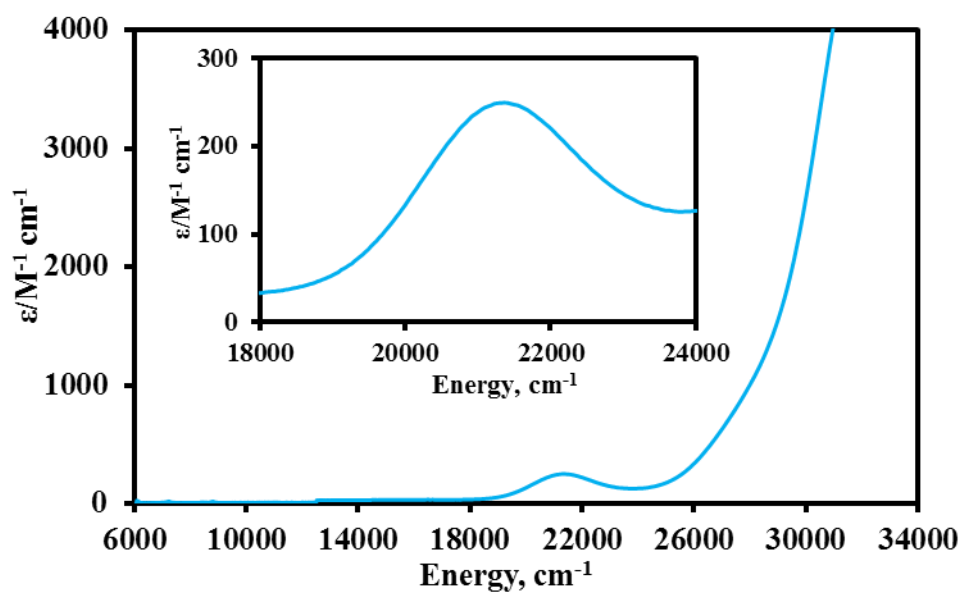


Figure S63. UV-vis-NIR spectrum of **3-Ce** between 34000–6000 cm^{-1} (295–1650 nm) recorded as a 0.5 mM solution in toluene.

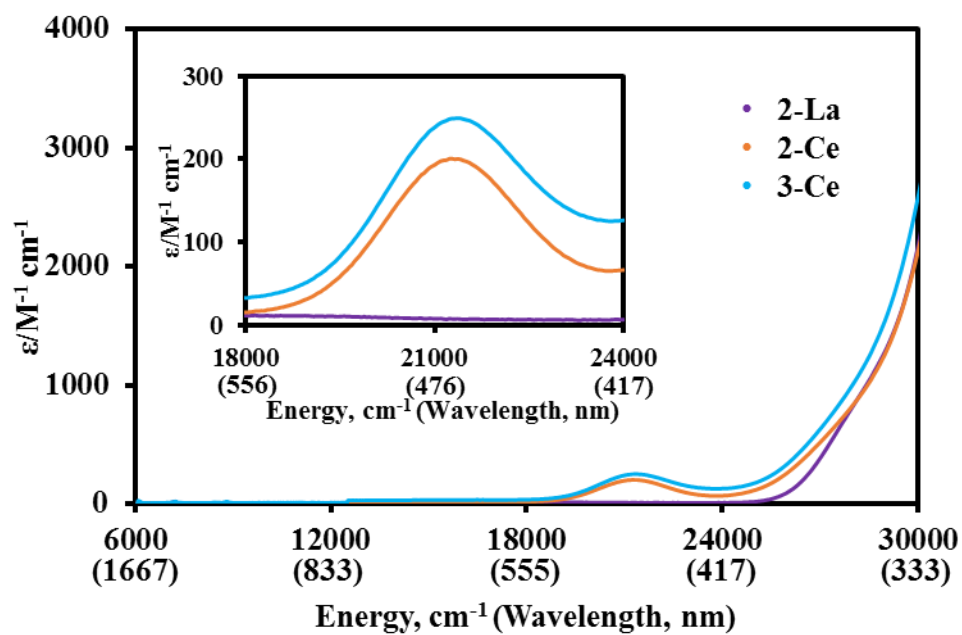


Figure S64. UV-vis-NIR spectrum of **2-La**, **2-Ce**, **3-Ce**, in the region 6000–30000 cm^{-1} (inset 18000–24000 showing main region) recorded in toluene at room temperature, concentrations listed above individually.

8. Magnetism

Magnetic measurements were performed using a Quantum Design MPMS-XL7 superconducting quantum interference device (SQUID) magnetometer. Separately, crystalline samples of **1-Ln** (Ln = Ce, Nd, Sm), **2-Ce** and **3-Ce** (30-50 mg) were crushed with a mortar and pestle under an inert atmosphere, and then loaded into borosilicate glass NMR tubes along with powdered eicosane (15-20 mg). The eicosane was melted by heating the tube gently with a low-power heat gun in order to immobilize the crystallites. The NMR tubes were then evacuated and flame-sealed to a length of *ca.* 5 cm. The NMR tubes were then mounted in the centre of drinking straws using friction by wrapping them with Kapton tape, and the straws were then fixed to the end of the sample rod. The measurements were corrected for the diamagnetism of the straw, borosilicate tube and eicosane using calibrated blanks, and the intrinsic diamagnetism of the sample using Pascals constants.⁹

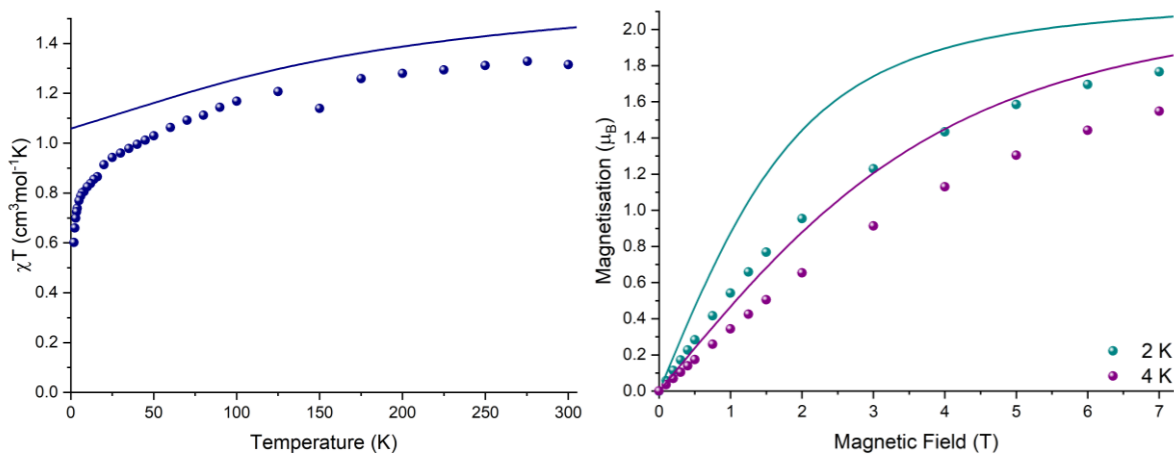


Figure S65. (left) Variable-temperature magnetic susceptibility of **1-Ce** in a 0.1 T static magnetic field; (right) Field dependence of the isothermal magnetisation curves at 2 K and 4 K, with experimental data points and CASSCF prediction (solid lines). Note that the data point at 150 K is a spurious outlier.

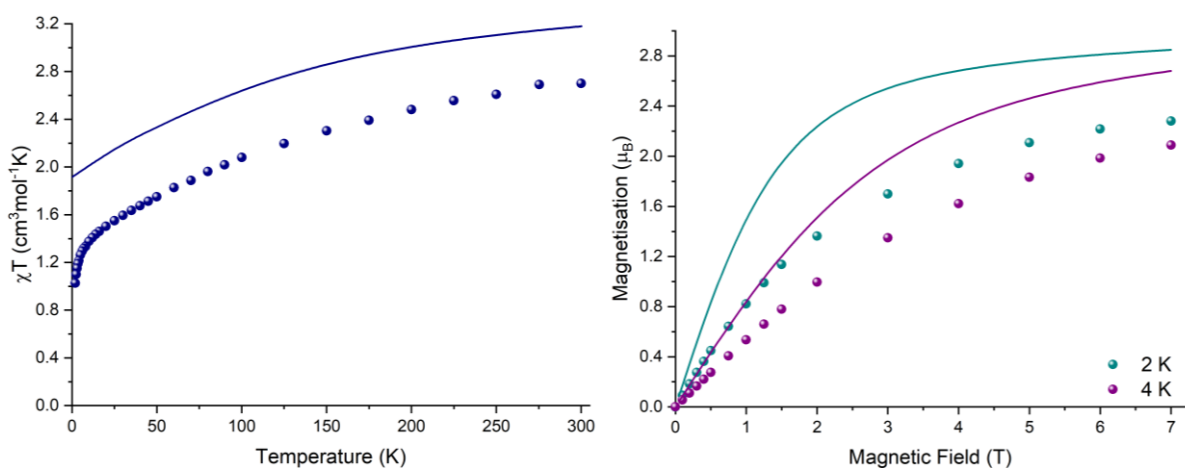


Figure S66. (left) Variable-temperature magnetic susceptibility of **1-Nd** in a 0.1 T static magnetic field; (right) Field dependence of the isothermal magnetisation curves at 2 K and 4 K, with experimental data points and CASSCF prediction (solid lines).

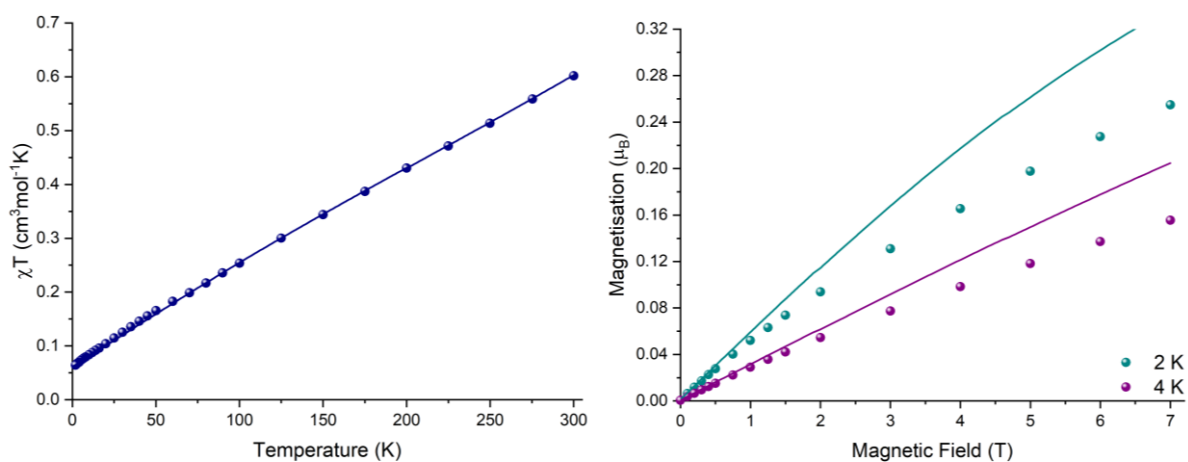


Figure S67. (left) Variable-temperature magnetic susceptibility of **1-Sm** in a 0.1 T static magnetic field; (right) Field dependence of the isothermal magnetisation curves at 2 K and 4 K, with experimental data points and CASSCF prediction (solid lines).

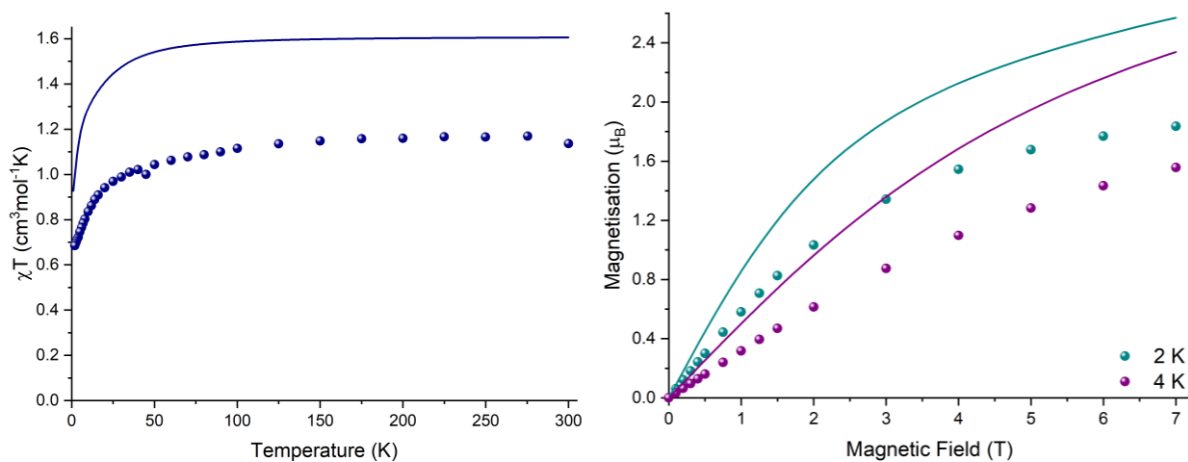


Figure S68. (left) Variable-temperature magnetic susceptibility of **2-Ce** in a 0.1 T static magnetic field; (right) Field dependence of the isothermal magnetisation curves at 2 K and 4 K, with experimental data points and CASSCF prediction (solid lines). Note that the data point at 50 K is a spurious outlier.

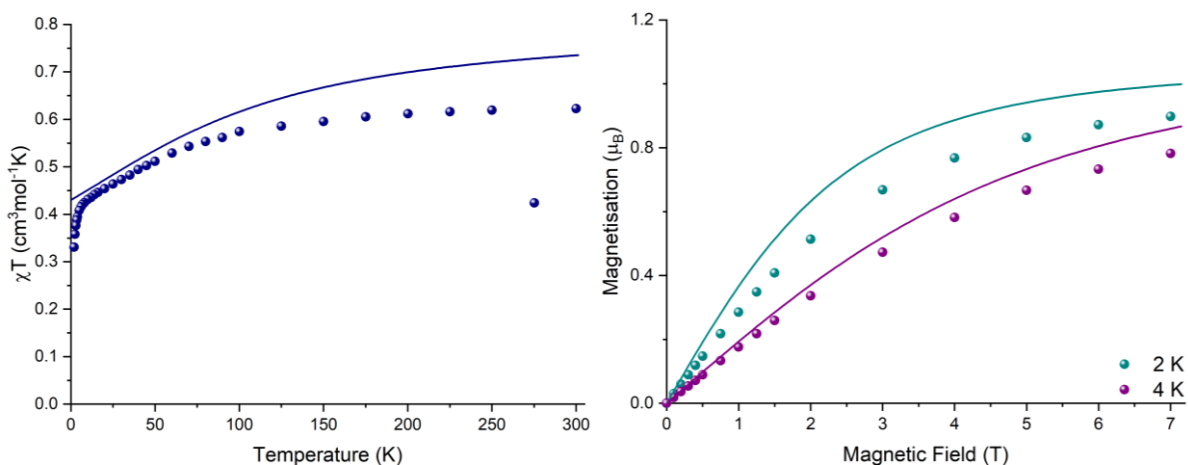


Figure S69. (left) Variable-temperature magnetic susceptibility of **3-Ce** in a 0.1 T static magnetic field; (right) Field dependence of the isothermal magnetisation curves at 2 K and 4 K, with experimental data points and CASSCF prediction (solid lines). Note that the data point at 275 K is a spurious outlier.

9. CASSCF-SO results

Complete active space self-consistent field spin orbit (CASSCF-SO) calculations were performed using MOLCAS 8.0¹⁰ with the single crystal X-ray structures of [Ln(Htp)₂(μ-BH₄)₂] (1-Ln; Ln = Ce, Nd, Sm), [Ln(Htp)₂(μ-BH₄)₂K(S)₂]_n (2-Ln; Ln = Ce, S = DME, n = 2; 3-Ce, Ln = Ce, S = Et₂O and THF, n = ∞) and [Ce(Cp^{tt})₂(μ-BH₄)₂] (4-Ce). The bimetallic molecular systems employed a La³⁺ ion as substitution for the ion not in focus of the calculation. The central Ln³⁺ ion was described using the ANO-RCC VTZP quality basis, with the first coordination sphere described using VDZP and all other atoms using VDZ quality.¹¹ The two electron integrals were decomposed using the Cholesky approach with a threshold of 10⁻⁸. The active space incorporated the 1, 3 and 5 active 4f electrons of Ce³⁺, Nd³⁺ and Sm³⁺ respectively, in the seven 4f orbitals. State-averaged CASSCF calculations for Ce were performed on the 7 doublet spin states with all states mixed by SO coupling in the RASSI routine. For Nd CASSCF was performed on 35 quartets and 112 doublets, with all states incorporated in the RASSI routine. For Sm CASSCF was performed on 21 sextets, 224 quartets and 490 doublets, where only 21 sextets, 128 quartets and 130 doublets were incorporated in the SO coupling treatment using the RASSI routine. The CFPs were extracted using Single_Aniso where the quantisation axis was the principal g_z-value of the ground Kramers doublet.¹²

Table S5. Crystal field states of the ground ²F_{5/2} for 1-Ce (Ce(1) with Htp_{cent} = 2.605(6) Å, P atoms relatively close to BH₄⁻ moieties).

Energy (cm ⁻¹)	Energy (K)	g _x	g _y	g _z	g _z angle (degrees)	Wavefunction
0.00	0.00	0.46	0.65	4.04	--	97.7 ±5/2>, 1.9 ±3/2>, 0.4 ±1/2>
276	397	1.48	1.83	2.10	88.00	2.2 ±5/2>, 71.0 ±3/2>, 26.8 ±1/2>
626	901	0.10	0.14	3.81	88.53	0.1 ±5/2>, 27.1 ±3/2>, 72.8 ±1/2>

Table S6. Crystal field states of the ground $^2F_{5/2}$ for **1-Ce** (Ce(2) with $H_{\text{tp}_{\text{cent}}} = 2.626(6) \text{ \AA}$, P atoms far away from BH_4^- moieties).

Energy (cm^{-1})	Energy (K)	g_x	g_y	g_z	g_z angle (degrees)	Wavefunction
0.00	0.00	0.33	0.61	4.05	--	$97.1 \pm 5/2\rangle, 1.0 \pm 3/2\rangle, 1.9 \pm 1/2\rangle$
394	567	0.90	1.81	1.94	31.97	$2.1 \pm 5/2\rangle, 86.0 \pm 3/2\rangle, 11.9 \pm 1/2\rangle$
892	1283	0.40	1.07	3.72	88.31	$0.9 \pm 5/2\rangle, 12.9 \pm 3/2\rangle, 86.2 \pm 1/2\rangle$

Table S7. Crystal field states of the ground $^4I_{9/2}$ for **1-Nd** (Nd(1), P atoms relatively close to BH_4^- moieties).

Energy (cm^{-1})	Energy (K)	g_x	g_y	g_z	g_z angle (degrees)	Wavefunction
0	0	0.27	0.41	5.12	--	$67.3 \pm 9/2\rangle, 0.3 \pm 7/2\rangle, 21.3 \pm 5/2\rangle, 2.3 \pm 3/2\rangle, 8.8 \pm 1/2\rangle$
81	116	0.72	1.08	2.94	5.16	$0.4 \pm 9/2\rangle, 43.0 \pm 7/2\rangle, 7.7 \pm 5/2\rangle, 47.7 \pm 3/2\rangle, 1.2 \pm 1/2\rangle$
179	257	0.08	1.10	4.10	0.46	$31.2 \pm 9/2\rangle, 1.1 \pm 7/2\rangle, 56.3 \pm 5/2\rangle, 2.4 \pm 3/2\rangle, 8.9 \pm 1/2\rangle$
331	476	0.14	1.69	4.86	77.54	$0.9 \pm 9/2\rangle, 40.7 \pm 7/2\rangle, 9.4 \pm 5/2\rangle, 16.3 \pm 3/2\rangle, 32.7 \pm 1/2\rangle$
385	553	0.86	2.61	4.14	89.99	$0.1 \pm 9/2\rangle, 14.9 \pm 7/2\rangle, 5.3 \pm 5/2\rangle, 31.3 \pm 3/2\rangle, 48.3 \pm 1/2\rangle$

Table S8. Crystal field states of the ground $^4I_{9/2}$ for **1-Nd** (Nd(2), P atoms far away from BH_4^- moieties).

Energy (cm^{-1})	Energy (K)	g_x	g_y	g_z	g_z angle (degrees)	Wavefunction
0	0	0.33	0.48	5.87	--	$85.1 \pm 9/2\rangle, 1.6 \pm 7/2\rangle, 6.8 \pm 5/2\rangle, 2.6 \pm 3/2\rangle, 4.0 \pm 1/2\rangle$
98	142	0.85	3.02	3.40	89.99	$1.7 \pm 9/2\rangle, 51.5 \pm 7/2\rangle, 19.5 \pm 5/2\rangle, 24.0 \pm 3/2\rangle, 3.3 \pm 1/2\rangle$
209	301	0.46	2.05	4.57	90.00	$12.2 \pm 9/2\rangle, 7.7 \pm 7/2\rangle, 45.0 \pm 5/2\rangle, 11.4 \pm 3/2\rangle, 23.8 \pm 1/2\rangle$
361	519	0.37	0.46	5.33	53.68	$0.1 \pm 9/2\rangle, 33.9 \pm 7/2\rangle, 9.6 \pm 5/2\rangle, 39.2 \pm 3/2\rangle, 17.2 \pm 1/2\rangle$
393	566	0.61	2.46	4.58	76.12	$0.9 \pm 9/2\rangle, 5.4 \pm 7/2\rangle, 19.1 \pm 5/2\rangle, 22.8 \pm 3/2\rangle, 51.7 \pm 1/2\rangle$

Table S9. Crystal field states of the ground $^6H_{5/2}$ for **1-Sm** (Sm(1) with $\text{Htp}_{\text{cent}} = 2.544(6)$ Å, P atoms relatively close to BH_4^- moieties).

Energy (cm^{-1})	Energy (K)	g_x	g_y	g_z	g_z angle (degrees)	Wavefunction
0	0	0.13	0.37	0.97	--	$2.1 \pm 5/2\rangle, 27.5 \pm 3/2\rangle, 70.4 \pm 1/2\rangle$
191	275	0.45	0.54	0.94	87.93	$0.1 \pm 5/2\rangle, 72.1 \pm 3/2\rangle, 27.8 \pm 1/2\rangle$
394	567	0.01	0.09	2.02	88.11	$97.8 \pm 5/2\rangle, 0.4 \pm 3/2\rangle, 1.8 \pm 1/2\rangle$

Table S10. Crystal field states of the ground $^6H_{5/2}$ for **1-Sm** (Sm(2) with $\text{Htp}_{\text{cent}} = 2.578(7)$ Å, P atoms far away from BH_4^- moieties).

Energy (cm^{-1})	Energy (K)	g_x	g_y	g_z	g_z angle (degrees)	Wavefunction
0	0	0.12	0.13	0.91	--	$4.5 \pm 5/2\rangle, 35.7 \pm 3/2\rangle, 59.8 \pm 1/2\rangle$
263	379	0.34	0.63	0.77	90.00	$5.1 \pm 5/2\rangle, 63.7 \pm 3/2\rangle, 31.2 \pm 1/2\rangle$
460	662	0.19	0.32	1.99	89.26	$90.4 \pm 5/2\rangle, 0.7 \pm 3/2\rangle, 9.0 \pm 1/2\rangle$

Table S11. Crystal field states of the ground $^2F_{5/2}$ for **2-Ce**.

Energy (cm ⁻¹)	Energy (K)	g _x	g _y	g _z	g _z angle (degrees)	Wavefunction
0	0	0.24	0.47	3.46	--	84.6 ±5/2), 3.6 ±3/2), 11.7 ±1/2)
44	64	0.20	0.83	3.13	72.02	2.9 ±5/2), 42.9 ±3/2), 54.2 ±1/2)
285	410	0.54	0.94	3.02	85.22	12.4 ±5/2), 53.5 ±3/2), 34.1 ±1/2)

Table S12. Crystal field states of the ground $^2F_{5/2}$ for **3-Ce**.

Energy (cm ⁻¹)	Energy (K)	g _x	g _y	g _z	g _z angle (degrees)	Wavefunction
0	0	0.86	1.15	3.42	--	87.3 ±5/2), 7.5 ±3/2), 5.2 ±1/2)
127	183	0.25	0.42	3.68	85.57	5.0 ±5/2), 23.3 ±3/2), 71.8 ±1/2)
320	460	0.80	1.25	2.80	87.39	0.1 ±5/2), 27.1 ±3/2), 72.8 ±1/2)

Table S13. Crystal field states of the ground $^2F_{5/2}$ for **4-Ce site A (Ce1)**.

Energy (cm ⁻¹)	Energy (K)	g _x	g _y	g _z	g _z angle (degrees)	Wavefunction
0	0	0.66	1.24	3.70	--	90.3 ±5/2), 4.7 ±3/2), 5.0 ±1/2)
212	305	0.96	1.29	2.45	88.65	9.3 ±5/2), 62.4 ±3/2), 28.3 ±1/2)
677	974	0.04	0.34	3.84	89.67	0.4 ±5/2), 33.0 ±3/2), 66.6 ±1/2)

Table S14. Crystal field states of the ground $^2F_{5/2}$ for **4-Ce site B (Ce2)**.

Energy (cm ⁻¹)	Energy (K)	g _x	g _y	g _z	g _z angle (degrees)	Wavefunction
0	0	0.53	0.91	3.90	--	93.9 ±5/2), 2.5 ±3/2), 3.5 ±1/2)
193	277	1.26	1.50	2.31	85.59	5.5 ±5/2), 67.5 ±3/2), 27.0 ±1/2)
642	923	0.17	0.24	3.88	89.00	0.6 ±5/2), 30.0 ±3/2), 69.5 ±1/2)

10. References

1. *CrysAlisPRO*, Version 39.27b; Agilent Technologies: Yarnton, U.K., 2017.
2. G. M. Sheldrick, *Acta Crystallogr. Sect. A*, 2008, **64**, 112.
3. G. M. Sheldrick, *Acta Crystallogr. Sect. C*, 2015, **71**, 3.
4. O. V. Dolomanov, L. J. Bourhis, R. J. Gildea, J. A. K. Howard and H. Puschmann, *J. Appl. Crystallogr.*, 2009, **42**, 339.
5. L. J. Farrugia, *J. Appl. Crystallogr.*, 2012, **45**, 849.
6. *POV-Ray*, Persistence of Vision Raytracer Pty. Ltd.: Williamstown, Australia, 2013.
7. *MestReNova*, Version 14.1.0-24037, Mestralab Research S.L.: Compostela, Spain, 2019.
8. F. P. Gasparro, *J. Chem. Educ.* 1977, **54**, 258.
9. G. A. Bain and J. F. Berry, *J. Chem. Ed.*, 2008, **85**, 532.
10. F. Aquilante, J. Autschbach, R. K. Carlson, L. F. Chibotaru, M. G. Delcey, L. De Vico, I. Fernandez Galván, N. Ferré, L. M. Frutos, L. Gagliardi, M. Garavelli, A. Giussani, C. E. Hoyer, G. Manni, H. Lischka, D. Ma, P. Å. Malmqvist, T. Müller, A. Nenov, M. Olivucci, T. B. Pedersen, D. Peng, F. Plasser, B. Pritchard, M. Reiher, I. Rivalta, I. Schapiro, J. Segarra-Martí, M. Stenrup, D. G. Truhlar, L. Ungur, A. Valentini, S. Vancoillie, V. Veryazov, V. P. Vysotskiy, O. Weingart, F. Zapata and R. Lindh, *J. Comput. Chem.*, 2016, **37**, 506.
11. (a) B. O. Roos, R. Lindh, P.-Å. Malmqvist, V. Veryazov and P.-O. Widmark, *J. Phys. Chem. A*, 2004, **108**, 2851; (b) B. O. Roos, R. Lindh, P.-Å. Malmqvist, V. Veryazov and P.-O. Widmark, *J. Phys. Chem. A*, 2005, **109**, 6575.
12. L. Ungur and L. F. Chibotaru, *Chem. Eur. J.*, 2017, **23**, 3708